Chemical responses to hydraulic fracturing and wolframite precipitation in the vein-type tungsten deposits of southern China

Xiangchong Liu[a,b], Yue Ma[c], Huilin Xing[d], Dehui Zhang[c,*]

[a] Institute of Geomechanics, Chinese Academy of Geological Sciences, Beijing 100081, China
[b] The Laboratory of Dynamic Digenesis and Metallogenesis, Institute of Geomechanics, CAGS, China
[c] State Key Laboratory of Geological Processes and Mineral Resources, School of Earth Sciences and Resources, China University of Geosciences (Beijing), Beijing 100083, China
[d] Centre for Geoscience Computing, School of Earth and Environmental Sciences, The University of Queensland, Brisbane, QLD 4072, Australia

ARTICLE INFO

ABSTRACT

Wolframite is the main ore mineral in the vein-type tungsten deposits of southern China. Much progress has been made on the characteristics of the mineralizing fluids, but the mechanisms of wolframite precipitation remain poorly understood. Hydraulic fracturing driven by high-pressure fluids is a common mechanical process during magmatic-hydrothermal transition, but it is uncertain whether and how this mechanical process may affect chemical equilibrium and cause wolframite precipitation. This paper examines how a hydraulic fracturing process affects solubility of tungsten in CO_2-saturated NaCl solutions using a hydro-mechanical numerical model coupled with a multi-component thermodynamic model. The thermodynamic model presented here is in the system of Fe-W-Cl-Na-C-O-H. The modeling results indicate that fluid pressure exerts a significant influence on chemical equilibrium where CO_2 solubility in NaCl solutions decreases with decreasing fluid pressure and pH increases with decreasing fluid pressure. An increase in pH reduces the concentrations of the dominant iron-bearing species ($FeCl_2^0$) and the dominant tungsten-bearing species (HWO_4^-) in fluids. Tungsten solubility in fluids reaches tens of ppm. Over ten fluctuations of fluid pressure are identified in the numerical experiments of hydraulic fracturing. These pressure fluctuations cause a decrease in solubility of tungsten by over 30% of the maximum solubility. Repeated drops of fluid pressure during hydraulic fracturing processes cause CO_2 loss and could be efficient processes for precipitating wolframite from mineralizing fluids. These findings may also offer an insight into the precipitation mechanisms of other metals from CO_2-bearing hydrothermal fluids.

1. Introduction

Magmatic-hydrothermal fluids are efficient agents of metal transport and form ore deposits with economically exploitable tungsten, tin, copper, and gold (Černý et al., 2005). How these metals are precipitated from magmatic-hydrothermal fluids is critical for understanding the ore forming processes (e.g. Audétat et al., 1998; Heinrich, 1990; Heinrich et al., 2005; Seward, 1997; Williams-Jones and Migdisov, 2013). Mixing of magmatic fluids and meteoric fluids is an efficient way to precipitate ore minerals (e.g. Audétat et al., 1998; Fekete et al., 2016; Heinrich, 2007). However, release of hydrothermal fluids from a volatile-rich magma suppresses free convection and prevents meteoric fluids from mixing with magmatic fluids close to the magma (e.g. Gerdes et al., 1998; Hanson, 1995; Weis et al., 2012). In this case, other possible mechanisms of precipitating ore minerals include simple cooling, phase separation, fluid-rock interaction, and hydraulic fracturing (e.g. Gibert et al., 1992; Korges et al., 2017; Lecumberri-Sanchez et al., 2017; Ni et al., 2015; Polya, 1990). The efficiency of metal precipitation reached by simple cooling is severely limited by the low rate of heat transfer to surrounding rock (Barton and Toulmin, 1961; Heinrich et al., 2005). Phase separation is generally triggered in shallower hydrothermal systems where fluid pressure decreases to the two-phase boundary (e.g. Korges et al., 2017). Fluid-rock interaction requires specific chemical disequilibrium between hydrothermal fluids and rocks (e.g. Lecumberri-Sanchez et al., 2017). Hydraulic fracturing may also cause metal precipitation from CO_2-bearing hydrothermal fluids (e.g. Polya, 1990), but it remains poorly understood how this fluid-driven mechanical process affects chemical equilibrium.

Wolframite is the main ore mineral in the vein-type tungsten deposits of southern China, which is a world-class tungsten province (Mao

et al., 2013). How wolframite in these deposits is precipitated from hydrothermal fluids is highly disputed (e.g. Ni et al., 2015; Wei et al., 2012; Xiong et al., 2017). Wei et al. (2012) proposed that mixing of magmatic fluids and meteoric fluids is the dominant mechanism for precipitating the wolframite in the Xihuashan tungsten deposit. However, many other hydrogen and oxygen isotopic measurements suggest that the mineralizing fluids were not mixed with meteoric fluids at the main mineralization stage (e.g. Gong et al., 2015; Liu et al., 2011; Mu et al., 1981; Wang et al., 2007; Zhu et al., 2015). Ni et al. (2015) argued that simple cooling caused precipitation of wolframite, but heat transfer from hydrothermal fluids to wallrock is too slow to precipitate wolframite efficiently (cf. Barton and Toulmin, 1961). The third mechanism is CO_2 escaping and pH increase (Wang et al., 2012; Wang et al. 2013b; Xiong et al., 2017). Recent infrared micro-thermometric studies found CO_2 from fluid inclusions in wolframite (e.g. Chen et al., 2018; Li et al., 2018). Previous structural and geochemical studies suggest high-pressure fluids are required for triggering fracture initiation and propagation and the fluctuations of fluid pressure are recorded by fluid inclusions (e.g. He and Xi, 1988; Wang et al., 2008; Xi et al., 2008; Yu, 2004). Thus, it is necessary to examine whether and how CO_2 loss accompanying a decrease in fluid pressure causes precipitation of wolframite.

The thermodynamic model proposed by Wood and Samson (2000) provides a fundamental understanding of the solubilities of ferberite and scheelite in CO_2-free aqueous NaCl solutions. In this study, a thermodynamic model including CO_2 and its reactions in NaCl aqueous solutions was developed. An important difference from the results in Wood and Samson (2000) is that tungsten solubility in the models presented here decreases with fluid pressure. It was found that fluid pressure fluctuations during a hydraulic fracturing process could precipitate a great part of tungsten dissolved in hydrothermal fluids.

2. Geological background

The South China tectonic block (SCB) consists of the Cathaysian Block and the Yangtze Craton (Fig. 1). The tectonic setting in the SCB was largely under extension during the Late Mesozoic (J_2-K_2) (Zhou et al., 2006), during which time NE-trending extensional lithospheric belts and deep faults controlled large-scale magmatic activities and related tungsten mineralization (Huang and Jiang, 2014; Mao et al., 2013; Zhao et al., 2017b). The tungsten mineralization in this region is dominated by quartz-vein, skarn, and greisen types (Zhao et al., 2017b). The vein-type tungsten deposits are the subject of this study.

The tungsten-bearing quartz veins are hosted by the Neoproterozoic to Jurassic strata and granitic rocks and extend a depth of approximately 1000 m (see Fig. 2) (Gu, 1984; Zhu et al., 1981). Wolframite is the main ore mineral in the veins (Fig. 3), and the gangue minerals have quartz, feldspar, muscovite, calcite, and tourmaline (Chen et al., 1989).
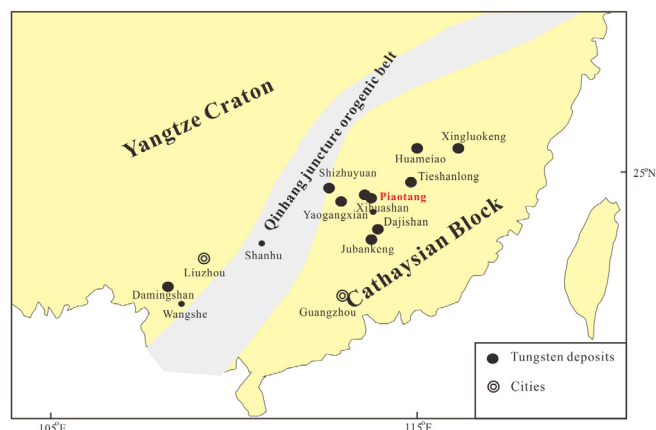

Fig. 1. Distribution of the tungsten deposits in southern China.

It is interpreted that the mineralizing fluids have a magmatic origin at the main mineralization stage, and then were mixed with meteoric waters at late stages (Zhu et al., 2014). A few lines of evidence suggest that these deposits may have a genetic relationship to highly fractionated granitoids at deeper levels (cf. Fang et al., 2015; Legros et al., 2018; Wang et al., 2017; Wu et al., 2017; Zhao et al., 2017b).

The quartz veins in most tungsten deposits are sub-verticall and have a preferred orientation of approximately east–west striking (Fig. 2) (Zhu et al., 1981). The sheeted veins often show a vertically morphological zonation that the thin veins at shallower levels become thicker downwards (Liu et al., 2014; Liu and Ma, 1993).

The mineralizing fluids are NaCl-$H_2O \pm CO_2$ systems. The fluid inclusions trapped by ore and gangue minerals have homogenization temperatures from 160 °C to 390 °C and salinities from 1 to 10 wt% NaCl equivalent. The mineralization pressures recorded by fluid inclusions have a range from 20 to 160 MPa with maximum range of 75–160 MPa (Gong et al., 2015; Liu et al., 2011; Mu et al., 1981; Ni et al., 2015; Wang et al., 2007; Wang et al. 2013a; Wei et al., 2012; Xi et al., 2008; Xiong et al., 2017; Zhou et al., 2017; Zhu et al., 2015). CO_2-bearing fluid inclusions are recorded in wolframite, topaz, and quartz (e.g. Chen et al., 2018; Li et al., 2018; Wang et al., 2012; Xi et al., 2008; Xiong et al., 2017; Zhou et al., 2017). Also, fluid inclusions in quartz have high concentrations of W, Fe, Mn, and other ore elements (Huang et al., 2013), suggesting that these inclusions have trapped the mineralizing fluids.

In the next sections, a thermodynamic model is established to examine how fluid pressure affects chemical equilibrium and tungsten solubility in NaCl-H_2O-CO_2 system. Wood and Samson (2000) proposed a thermodynamic mode for understanding the mechanisms precipitating ferberite and scheelite from CO_2-free NaCl solutions. Some reactions in their models and CO_2-related reactions are considered together in our models. A hydraulic fracturing process is also simulated to constrain the evolution of fluid pressure using finite element based numerical experiments.

3. Methods

3.1. Thermodynamic modeling of a W-bearing NaCl-H_2O-CO_2 system

3.1.1. Species and reactions in the models

Wolframite ([Fe,Mn]WO_4) in tungsten deposits in the world is often a complete solid solution between ferberite (FeWO_4) and hübnerite (MnWO_4) (e.g. Harlaux et al., 2018; Pačevski et al., 2007; Sakamoto, 1985; Tindle and Webb, 1989). Both Fe-dominated and Mn-dominated wolframite are identified in the vein-type tungsten deposits of southern China (e.g. Xie et al., 2017; Zhang, 1981; Zhang et al., 2018). Current thermodynamic data are insufficient to calculate the equilibrium constant of MnWO_4 dissolution (cf. Robie and Hemingway, 1995); thus, MnWO_4 was ignored and only the dissolution of FeWO_4 was considered in the models (see reaction 3 in Table 1). Since sheelite (CaWO_4) is a minor ore mineral in the vein-type tungsten deposits of southern China, CaWO_4 and Ca-related reactions are also absent in the models.

The main tungsten species in NaCl aqueous solutions are $H_2WO_4^0$, HWO_4^-, WO_4^{2-}, $NaHWO_4^0$, and $NaWO_4^-$ (Redkin and Kostromin, 2010; Wood and Samson, 2000). These species and their reactions with H^+ or Na^+ were incorporated in the models.

Hydrothermal fluids in the crust are generally of low oxidation potential, and dissolved Fe is predominantly in the $+2$ oxidation state (Heinrich and Seward, 1990). It is reported that the two-mica granite in the Dajishan tungsten deposit has an oxygen fugacity of $logf_{O_2} = -15$ (Jiang et al., 2004). The muscovite granite and the lepidolite granite in the Dahutang tungsten deposit have a lower oxygen fugacity $log\, f_{O_2} < -15$ (Han et al., 2016). Under these reduced conditions, the amount of Fe^{3+} in hydrothermal fluids is negligible compared to that of Fe^{2+} (cf. Wood and Samson, 2000). Thus, Fe^{2+} and its reactions with Cl^- and OH^- were considered in the models.
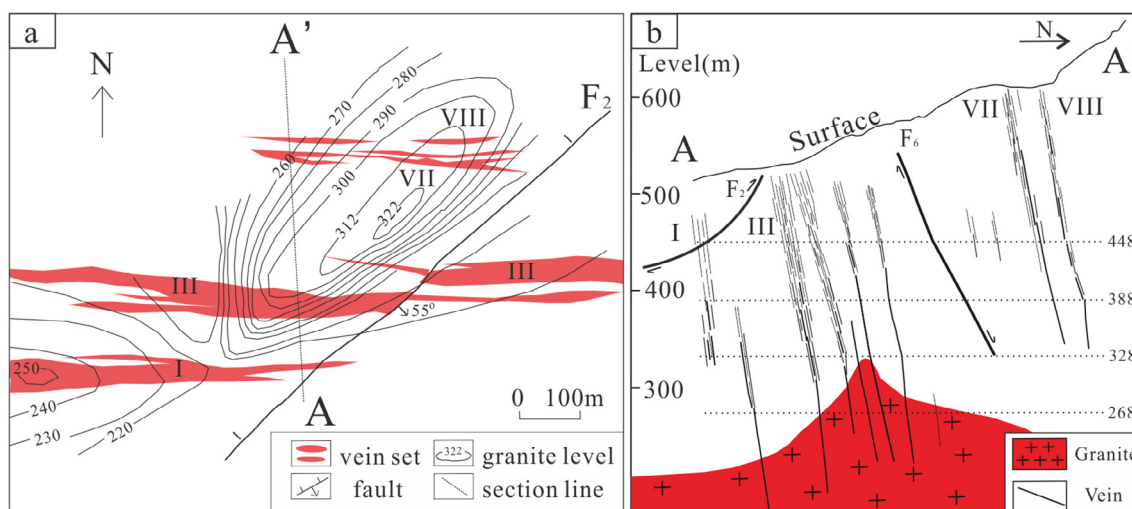
Fig. 2. (a) A planar view of the Piaotang tungsten deposit (revised from Shan, 1976); (b) A cross section of the Piaotang tungsten deposit along the section line A-A' in Fig. 1a.

Species of oxidized carbon dissolved in water are dominated by carbonate ion (CO_3^{2-}), bicarbonate ion (HCO_3^-), and dissolved CO_2 (aq) (Manning et al., 2013). These oxidized carbon species interact via two stepwise dissociation reactions (see reactions 15 and 16 in Table 1).

21 species and 16 reactions in aqueous solutions were investigated in the models (Table 1). 21 equations were required to be solved for determining the concentration of the 21 species. The equilibrium constants of the 16 reactions in Table 1 were calculated using the R package CHNOSZ developed by Dick (2017). Thus, 16 non-linear equations were established from these 16 reactions. The other five equations were obtained from the charge and mass balance (Table 2). Note that species concentrations were used in the balance equations and species activities were used in the reactions (see Section 3.1.2). The last equation in Table 2 was established based on the assumption that CO_2 in NaCl solutions was saturated. The CO_2-bearing three-phase fluids inclusions (liquid water, liquid CO_2, and gaseous CO_2) at room temperature have been identified in several vein-type tungsten deposits of southern China (e.g. Wang et al., 2012; Xi et al., 2008; Xiong et al., 2017; Zhou et al., 2017). The mole fractions of CO_2 in CO_2-bearing fluid inclusions in the Dajishan and Pangushan tungsten deposits have a range of 0.06–0.76 and 0.22–0.46, respectively (Wang et al., 2012; Xi et al., 2008). Fig. 4 shows the mole fraction of CO_2 in CO_2-saturated NaCl solutions under the temperature, pressure, and salinity conditions

Table 1
The equilibrium constants (LogK) of the 16 reactions employed in this study.

Number	Reaction	LogK (350 °C, 100 MPa)
1	$H^+ + HWO_4^- = H_2WO_4^0$	3.32
2	$H^+ + WO_4^{2-} = HWO_4^-$	6.88
3	$FeWO_4(s) = Fe^{2+} + WO_4^{2-}$	−15.21
4	$Fe^{2+} + Cl^- = FeCl^+$	2.34
5	$Fe^{2+} + 2Cl^- = FeCl_2^0$	4.55
6	$H^+ + Cl^- = HCl^0$	1.19
7	$Na^+ + Cl^- = NaCl^0$	0.79
8	$H_2O = H^+ + OH^-$	−10.66
9	$Na^+ + H_2O = NaOH^0 + H^+$	−10.25
10	$Fe^{2+} + H_2O = FeOH^+ + H^+$	−4.49
11	$Fe^{2+} + H_2O = FeO^0 + 2H^+$	−10.23
12	$Fe^{2+} + 2H_2O = HFeO_2^- + 3H^+$	−17.13
13	$Na^+ + HWO_4^- = NaHWO_4^0$	0.15
14	$Na^+ + WO_4^{2-} = NaWO_4^-$	2.93
15	$CO_2 (aq) + H_2O = HCO_3^- + H^+$	−8.30
16	$HCO_3^- = CO_3^{2-} + H^+$	−11.06

The LogK of the reaction 3 was calculated using the function and the thermodynamic data in Wood and Samson (2000).
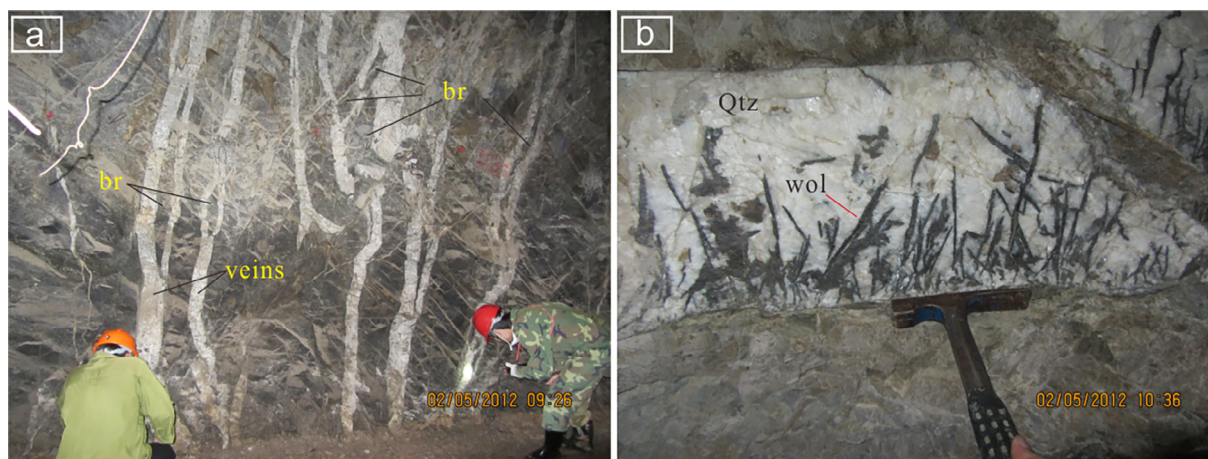

Fig. 3. Photos of the veins in the III vein set in the Piaotang tungsten deposit. (a) The subvertical veins at 328 m level have a thickness of 10–20 cm. These veins envelop breccias that were separated from surrounding wallrock. View to East. (b) Needle-like wolframite crystallized in a thick vein at 268 m level. View upwards. Abbreviations: br, breccias; Qtz, quartz; wol: wolframite.

Table 2
Mass and charge balance constraints used in the thermodynamic model.

Charge balance	$[H^+] + [Na^+] + [FeCl^+] + 2[Fe^{2+}] + [FeOH^+] = [HWO_4^-] + 2[WO_4^{2-}] + [Cl^-] + [OH^-] + [HFeO_2^-] + [HCO_3^-] + 2[CO_3^{2-}]$
Cl mass balance	$\Sigma Cl = [Cl^-] + [HCl^0] + [NaCl^0] + [FeCl^+] + 2[FeCl_2^0]$
Na mass balance	$\Sigma Na = [Na^+] + [NaCl^0] + [NaOH^0] + [NaWO_4^-] + [NaHWO_4^0]$
Stoichiometric dissolution ($\Sigma Fe = \Sigma W$)	$[H_2WO_4^0] + [HWO_4^-] + [WO_4^{2-}] = [FeCl^+] + [FeCl_2^0] + [Fe^{2+}] + [FeOH^+] + [FeO^0] + [HFeO_2^-]$
Fix CO_2	CO_2 reaches the solubility at the given temperature, pressure, and salinity

CO_2 solubility in NaCl aqueous solutions was reproduced using the model proposed by Mao et al. (2013).

of mineralizing fluids in the vein-type tungsten deposits of southern China. The mole fractions of CO_2 are generally lower than 0.4. Thus, the assumption of CO_2 saturation in hydrothermal fluids is plausible. CO_2 solubility in NaCl aqueous solutions was reproduced from the CO_2 solubility model proposed by Mao et al. (2013). These 21 nonlinear equations were solved using the R package rootSolve developed by Soetaert (2016).

3.1.2. Activity coefficients of charged and neutral species

The activity of a species in electrolyte solutions is its effective concentration and equals its concentration multiplied by its activity coefficient. The activity coefficients of electrically charged species in NaCl aqueous solutions are often calculated by an extended Deby-Hückel equation (B-dot equation) proposed by Helgeson (1969) (e.g. Gibert et al., 1992; Mikucki, 1998; Wood and Samson, 2000):

$$log\gamma_i = \frac{-Az_i^2\sqrt{I}}{1 + \dot{a}B\sqrt{I}} + \dot{b}I \qquad (1)$$

in which γ_i is the activity coefficient of the ith ion, z_i is the charge number of the ion, I is the ionic strength, A and B are two parameters related to the dielectric constant and density of water, and $\dot{a}$ and $\dot{b}$ are temperature-dependent constants. The ionic strength of a solution is a function of the concentrations of all the ions in that solution:

$$I = \frac{1}{2}\sum_{i=1}^{n} c_i z_i^2 \qquad (2)$$

in which I is the molar ionic strength in mol/kg and c_i is the molar concentration of the ith ion. The only species-specific parameter required in equation (1) is the electrical charge. This treatment may be incorrect, but its errors are negligible compared to those caused by other sources (Zhu et al., 2017). Activity coefficients of charged species were calculated by the R package CHNOSZ (Dick, 2017). The ionic strength I had an initial value of half of the molar concentration of NaCl in solutions and was updated in an iterative method until the absolute error was less than 0.01.
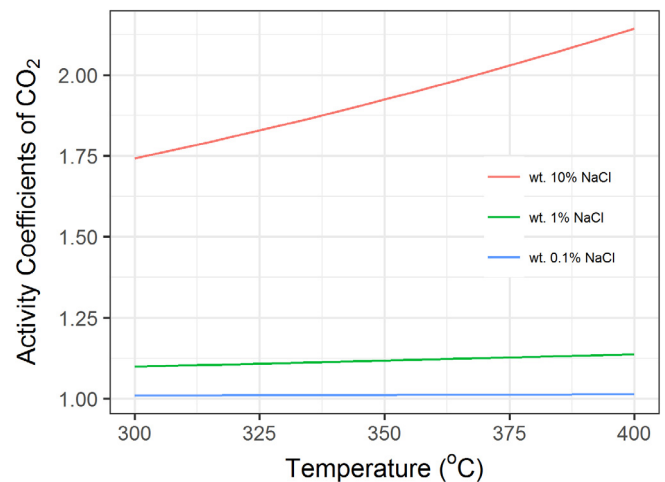
Fig. 5. Activity coefficients of CO_2 in NaCl aqueous solutions reproduced from the model developed by Drummond (1981).

Neutral species are considered to mix ideally in the solutions in Deby-Hückel type models (cf. Walther, 1997); therefore, activity coefficients of neutral aqueous species are often assumed to be unity (e.g. Gibert et al., 1992; Helgeson et al., 1981; Wood and Samson, 2000). However, when neutral species are high-concentration, the non-ideal interactions between neutral species and charged species may be considerable (cf. Walther, 1997). CO_2 is highly concentrated if CO_2 is saturated in NaCl aqueous solutions (see Fig. 4). The empirical equation fitted by Drummond (1981) was used to reproduce the activity coefficients of CO_2 (see equation A-10 in Spycher and Pruess, 2005). Fig. 5 shows that the activity coefficient of CO_2 tends to unity when the salinity approaches zero. The activity coefficients of the other neutral species in our models were assumed to unity given that reliable data for their activity coefficients are not available.
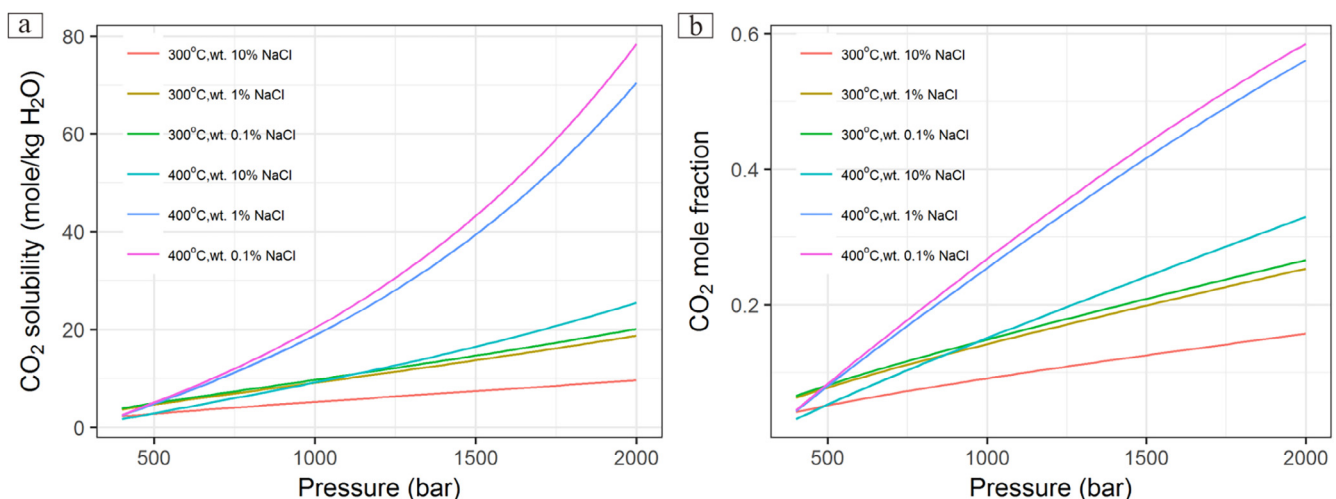
Fig. 4. The solubility (a) and mole fraction (b) of CO_2 in NaCl aqueous solutions reproduced from the model proposed by (Mao et al., 2013). The solubility of CO_2 decreases with increasing salinity of the solutions. This is called the salting-out effect (Dubacq et al., 2013; Nighswander et al., 1989).

3.2. Numerical modeling of hydraulic fracturing

Hydraulic fracturing is a fluid-to-solid coupling where a change in fluid pressure or fluid mass alters the volume of a porous material and produces strains (Wang, 2000). In the Navier-Coulomb criteria, rock failure occurs by hydraulic fracturing when the differential stress $\sigma_1-\sigma_3$ is less than four times tensile strength Ts and the effective minimum principle stress $\sigma_3' = \sigma_3-P$ reaches-Ts (Cosgrove, 1995; Cox, 2010; Sibson, 2004). σ_1, σ_2, and σ_3 denote the maximum principle stress, the intermediate principle stress, and the minimum principle stress, respectively. Positive normal stresses mean compression and negative normal stresses represent tension in this study. Hydraulic fracturing creates extensiontal fractures and veins and breccias in hydrothermal systems (e.g. Barnhoorn et al., 2010; Beach, 1980; Bons, 2001; Cosgrove, 2001; Cox, 2007; Jébrak, 1997; Plimer, 1987; Tsuchiya et al., 2016). The fluid pressure fluctuations after hydraulic fracturing may be recorded by fluid inclusions in veins (e.g. Rusk et al., 2004). Fracturing driven by high pressure fluids may also trigger earthquakes (e.g. Miller et al., 2004).

The orientation of the quartz veins in the tungsten deposits of southern China indicates that their tension direction is approximately north–south striking. Our previous study indicates that the maximum principle stress σ_1 was vertical and the intermediate principle stress σ_2 was east–west striking (Liu et al., 2014). Structural analysis of the vein arrays suggests that the initiation and propagation of the fractures were triggered by high-pressure fluids (e.g. He and Xi, 1988; Wang et al., 2008; Wei et al., 2015; Yu, 2004). In situ fragmentation textures in the veins (Fig. 3a) suggests that the brecciation is fluid-assisted (cf. Jébrak, 1997). Fluid inclusions from several tungsten deposits also record high-pressure fluids (e.g. Huang et al., 2006; Wang et al., 2007; Wang et al. 2013a Xi et al., 2008). Fluid-driven fracturing is modelled in this part to examine the change of fluid pressure during a hydraulic fracturing process and to be coupled to the thermodynamic model in Section 3.1.

The maximum pressures recorded in fluid inclusions were assumed to reach lithostatic pressure levels (25 MPa/km). Thus, the tungsten deposits in southern China may form at a depth of $3\sim6$ km. A two-dimension hydro-mechanical model at a depth of 4 km was built. The model has a size of 100 m x 100 m (Fig. 6). X axis represents the orientation normal to veins and Z axis is vertical. The coupling of rock deformation and fluid flow in this study was governed by poro-elastic constitutive equations and the diffusion equation of fluid pressure (see Appendix). These simultaneous partial differential equations were solved by an in-house finite element-based supercomputer simulator named PANDAS (Li and Xing, 2015; Liu et al., 2017a; Xing and Makinouchi, 2002). The yield criteria used in the models are the Maximum Tensile Stress Criterion and the Mohr-Coulomb Criterion (see Appendix).
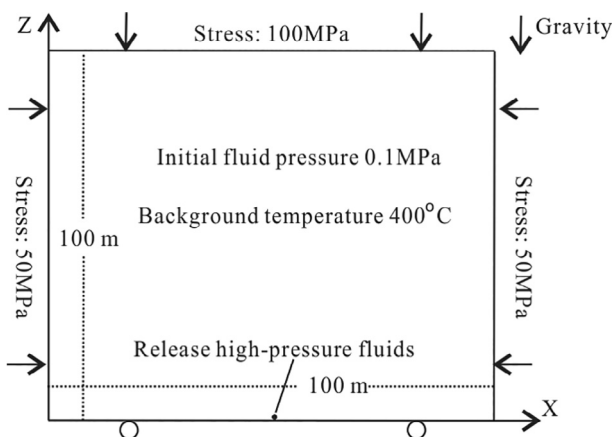

Fig. 6. A 2D geometric model of hydraulic fracturing at a depth of 4 km.

Isothermal fluids were assumed to be injected into the bottom of the models. The aim of this treatment is to save computational power and focus on the influence of fluid pressure on tungsten solubility. High-pressure fluids at 350 °C were used in the models and this temperature is within the homogenization temperatures of the tungsten deposits. The constitutive equations used in our models are independent on temperature (see Appendix).

The fluid physical properties required in the models include fluid density, compressibility, and viscosity. Mao et al. (2015) proposed a predictive model that reproduces the single-phase density of NaCl-H_2O-CO_2 fluid mixtures of all compositions from 273 to 1273 K and from 1 to 5000 bars within experimental uncertainty in most cases. Their model was used to reproduce the fluid density and fluid compressibility in our models. Current models for fluid viscosity of CO_2-bearing NaCl aqueous solutions are only valid at T ≤ 60 °C, P ≤ 300 bars (e.g. Bando et al., 2004; Fleury and Deschamps, 2009; Islam and Carlson, 2012; Kumagai and Yokoyama, 1999). Klyukin et al. (2017) developed an empirical model for the viscosity of H_2O-NaCl fluids at T ≤ 1000 °C, P ≤ 5000 bars, and salinity ≤100 wt% NaCl. Their model was used to reproduce the fluid viscosity in our models. Note that the fluid physical properties above were fixed to a constant level but were varied in different numerical experiments to examine their influences on hydraulic fracturing.

The fluids released from a CO_2-bearing magma are early low-salinity CO_2-rich fluids followed by more saline CO_2-free fluids (Baker, 2002; Holloway, 1976). The CO_2-bearing fluid inclusions in wolframite in the tungsten deposits have a salinity of 0.4–3.6 wt% NaCl equivalent (Chen et al., 2018; Li et al., 2018), and 1–6 wt% NaCl equivalent in quartz (Wang et al., 2012; Xi et al., 2008). The CO_2-free fluid inclusions have a salinity up to 10 wt% NaCl equivalent (e.g. Ni et al., 2015). Thus, a salinity of 10 wt% NaCl equivalent was used in the numerical experiments. This salinity is an upper limit of the fluid salinities above.

The quartz veins in the tungsten deposits of southern China are hosted by low-porosity sandstone and slate, granite (Li, 1993; Zhang et al., 2017; Zhao et al., 2017b). The rock in the models was assumed to be unfractured and had an initial permeability of 10^{-16} m^2. Equation (A-8) in Appendix shows that the rock permeability decreases with the effective normal stress before fracturing; therefore, the rock permeability before fracturing was lower than the minimum permeability (10^{-16} m^2) required for advective heat transport (cf. Manning and Ingebritsen, 1999). This treatment prevents heat transfer from hot fluids to the rock and is consistent with the assumption of isothermal fluids. The rock in our models has a Young's modulus of 60 GPa, a Poisson's ratio of 0.2, and a tensile strength of 5 MPa according to the experimental data in Pariseau (2006), Gercek (2007), and Lockner (1995), respectively. Table 3 shows the rock mechanical parameters and the fluid properties used in the numerical experiments.

The finite element based numerical experiments were run in two stages. At the first stage, a vertical compressive stress of 100 MPa (σ_v) was loaded at the top, a horizontal compressive stress of 50 MPa (σ_h) was loaded on the left and right sides of the model, and the bottom was fixed vertically (Fig. 1). This corresponds to a horizontal-over-vertical stress ratio of $\frac{\sigma_h}{\sigma_v}$ = 0.5. These boundary conditions formed an initial extensional stress field at a depth of 4 km if a lithostatic gradient of 25 MPa/km was assumed. At the second stage, the loaded stresses at the first stage were maintained and fluids with a fixed pressure of 200 MPa were released at the bottom. A small amount of fluids was assumed to exist in rocks before release of high-pressure magmatic fluids; thus the model was initially unsaturated and had an initial fluid pressure of 10 MPa. Fig. 7 shows the finite element meshes consisting of 39,200 elements and 59,643 nodes. A reference point shown in Fig. 7 was chosen to show the change of the effective minimum principle stress and the fluid pressure during a hydraulic fracturing process.

Six numerical experiments were conducted in this study and their parameters are shown in Table 3. Fluid properties at 350 °C, 200 MPa,

Table 3
Rock mechanical and hydraulic parameters in the numerical experiments.

Parameters(unit)	E1	E2	E3	E4	E5	E6
Porosity (%)	1.0					
Permeability (m2)	10^{-16}					
Young's Modulus (GPa)	60					
Poisson ratio	0.2					
Angle of internal friction (°)	30					
Cohesion (MPa)	60					
Tensile strength (MPa)	5					
Fluid temperature (°C)	350					
Fixed fluid pressure (MPa)	200					190
Horizontal stress (MPa)	50	50	50	50	55	50
CO_2 concentration (mol/kg H_2O)	14.92	7.46	14.92	14.92	14.92	14.92
Initial fluid pressure (MPa)	10	10	10	15	10	10
Fluid salinity (w.t.%)	10	10	–	10	10	10
Fluid density (kg/m^3)	883	899	883	883	883	850
Fluid viscosity (× 10^{-4}Pa•s)	1.28	1.28	1.41	1.28	1.28	1.28
Fluid compressibility (×10^{-10}Pa^{-1})	9.95	7.90	9.95	9.95	9.95	9.95

E1, E2, E3, E4, E5, E6 refer to the six numerical experiments.

and 10% wt% NaCl were used in the first numerical experiment (E1), which was the reference experiment. Only one variable in the next five numerical experiments (E2, E3, E4, E5, and E6) was varied based on E1 to examine the influences of fluid compressibility, fluid viscosity, the initial fluid pressure, the horizontal stress, and the fixed fluid pressure on hydraulic fracturing, respectively. The fluid pressure in the numerical experiments was linked to the thermodynamic mode to investigate how hydraulic fracturing affected chemical equilibrium and tungsten solubility in hydrothermal fluids.

4. Modeling results

4.1. Influences of fluid compressibility on hydraulic fracturing

CO_2 was saturated in the first numerical experiment (E1), while CO_2 concentration in the second one (E2) was half of CO_2 solubility in NaCl solutions at the same temperature, pressure, and salinity with E1. Fluids in E2 had a higher fluid density and a lower fluid compressibility than those in E1. Fluid density has a minor influence on hydraulic fracturing compared to fluid viscosity and fluid compressibility (e.g. Zhou and Burbey, 2014). Therefore, differences between E1 and E2 were made to

show the influences of fluid compressibility on hydraulic fracturing.

Fig. 8 shows that the effective minimum principle stress at the reference node decreased as fluid pressure increased in E1. The effective mean normal stress was initially compressive and increased with fluid pressure. The permeability at the reference node increased with the effective mean normal stress and was lower than 10^{-16} m^2 before fracturing. The effective minimum principle stress reached the tensile strength of 5 MPa after 2.7 s when fluid pressure reached 167.95 MPa. The peak fluid pressure reached at the time when the reference node yields is also called the breakdown pressure (Bunger et al., 2010). After fracturing, the permeability increased to 2×10^{-13} m^2 and the fluid pressure fluctuated significantly and decreased to 109.60 MPa after 2.8 s. In PANDAS, the stresses become zero once they reach the shear or tensile strength. In contrast, the tensile strength at the reference point in E2 was satisfied after 0.84 s, earlier than in E1. After fracturing, fluid pressure fluctuated from 156.33 MPa to 121.42 MPa.

4.2. Influences of fluid viscosity on hydraulic fracturing

The empirical model for fluid viscosity used in this study is independent on CO_2 concentration. Previous viscosity measurements of aqueous NaCl solutions with dissolved CO_2 suggests that fluid viscosity is positively correlated to CO_2 concentration (e.g. Bando et al., 2004). Thus, fluid viscosity in the third numerical experiment (E3) was increased by 10% based on that in E1 and the other parameters remained unchanged.

The effective minimum principle stress at the reference node in E3 was higher than that in E1 at any time before fracturing (Fig. 9). The tensile strength in E3 was satisfied after 3.0 s, later than that in E1. The fluid pressure at the reference node in E3 also shows significant fluctuations after fracturing. The breakdown pressure in E3 is 167.99 MPa, slightly higher than than in E1. Fluid pressure in E3 decreased to 87.91 MPa after 3.1 s.

4.3. Influences of the initial fluid pressure on hydraulic fracturing

The initial fluid pressure is another uncertain variable when high-pressure fluids are released. The initial fluid pressure in the fourth numerical experiment (E4) was increased to 15 MPa based on the first one and the other parameters kept unchanged.

The effective minimum principle stress at the reference node in E4 was always larger than that in E1 before fracturing and the tensile
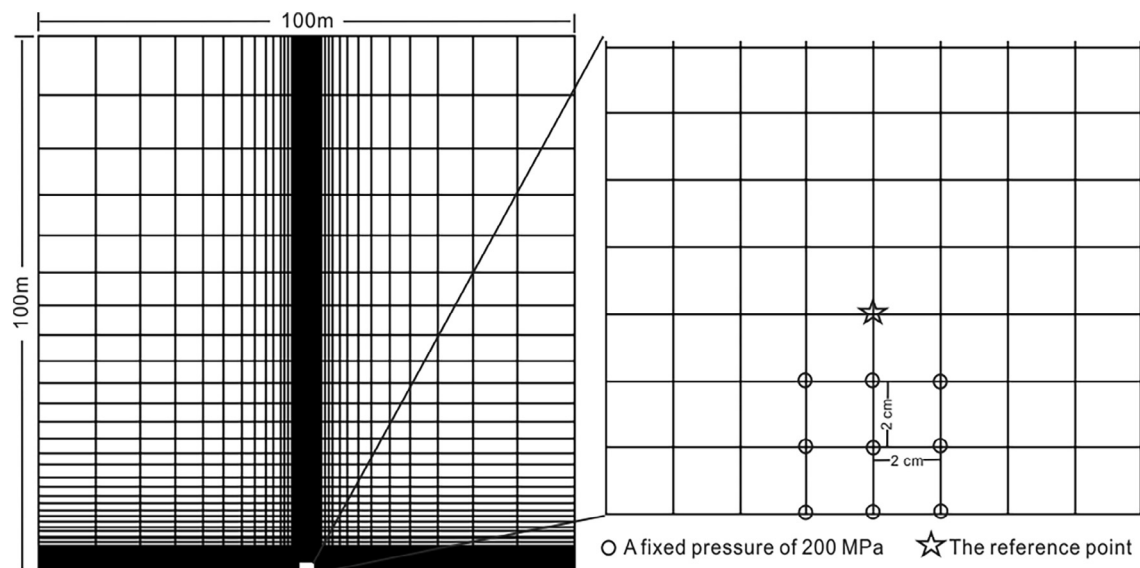

Fig. 7. The finite element meshes used in the numerical model of hydraulic fracturing. A reference node close to the fixed-pressure fluid source was chosen to illustrate the evolution of the stresses and the fluid pressure during a hydraulic fracturing process.
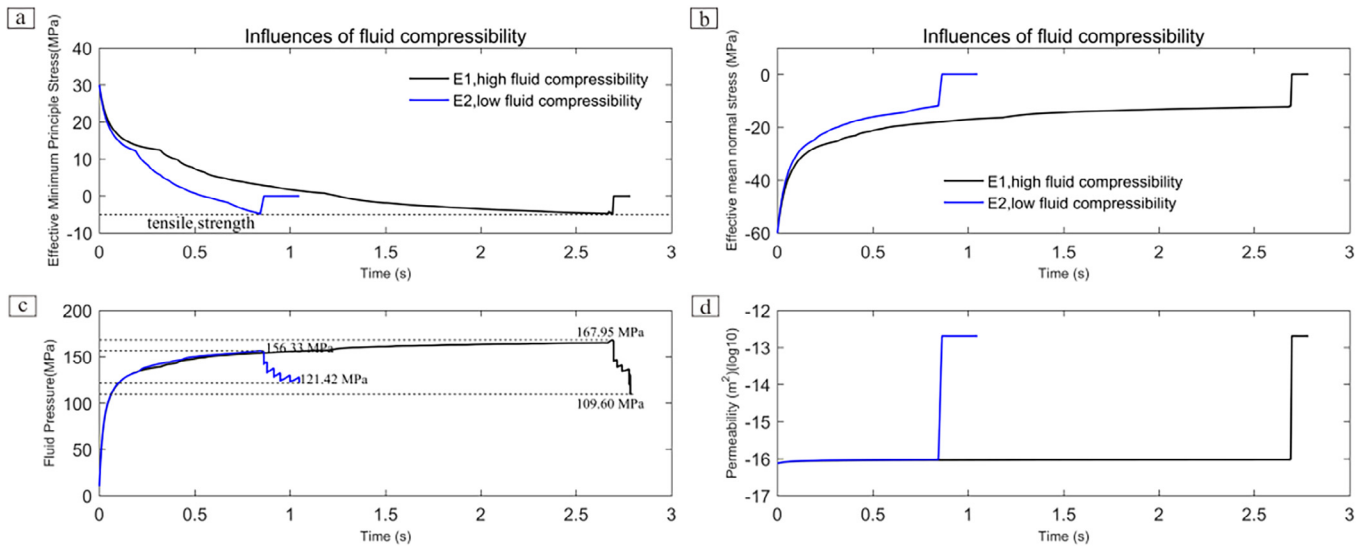
Fig. 8. The change of the effective minimum principle stress (a), the effective mean normal stress (b), the fluid pressure (c), and the permeability (d) at the reference node in the first (E1) and second (E2) numerical experiments. The only different variable between E1 and E2 was fluid compressibility. After the effective minimum principle stress reached the rock tensile strength of 5 MPa, the stresses became zero, the fluid pressure show a significant fluctuation, and the permeability increased by 2000 times. The tensile strength of the reference node was satisfied earlier in E2 than that in E1.

strength was satisfied after 3.3 s, later than that in E1 (Fig. 10). The breakdown pressure in E4 was 171.23 MPa, followed by significant fluctuations. The fluid pressure decreased to 120.90 MPa after 3.5 s.

4.4. Influences of the horizontal stress on hydraulic fracturing

The horizontal stress is a critical parameter affecting the initial stress field (e.g. Rutqvist et al., 2013). This parameter was increased to 55 MPa in the fifth numerical experiment (E5) to study how a higher horizontal stress affects hydraulic fracturing.

The reference node in E5 had a higher initial effective minimum principle stress than that in E1 (Fig. 11). The decrease of the effective minimum principle stress in E5 was slower than that in E1 and the tensile strength was satisfied after 7.2 s. The fluid pressure fluctuated from 175.15 MPa to 122.32 MPa.

4.5. Influences of the fixed fluid pressure on hydraulic fracturing

The last parameter analyzed in this study is the fixed fluid pressure at the bottom of the model. The fixed fluid pressure in the sixth numerical experiment (E6) was decreased to 190 MPa and the other parameters remained unchanged compared to those in E1.

The tensile strength of the reference node in E6 was satisfied after 4.4 s, later than that in E1 (Fig. 12). The breakdown pressure was 164.17 MPa and then the fluid pressure fluctuated to 92.01 MPa.

4.6. Chemical equilibrium of a tungsten-bearing NaCl-H_2O-CO_2 system

Three concentrations of CO_2 in NaCl solutions at 350 °C were used in solving the nonlinear equations in Section 3.1. The first concentration is CO_2 solubility, the second one is 50% of CO_2 solubility, and the third is 10% of CO_2 solubility (Fig. 13). pH varies from 3.3 to 4.7 and decreases with increasing fluid pressure and the concentration of CO_2 in
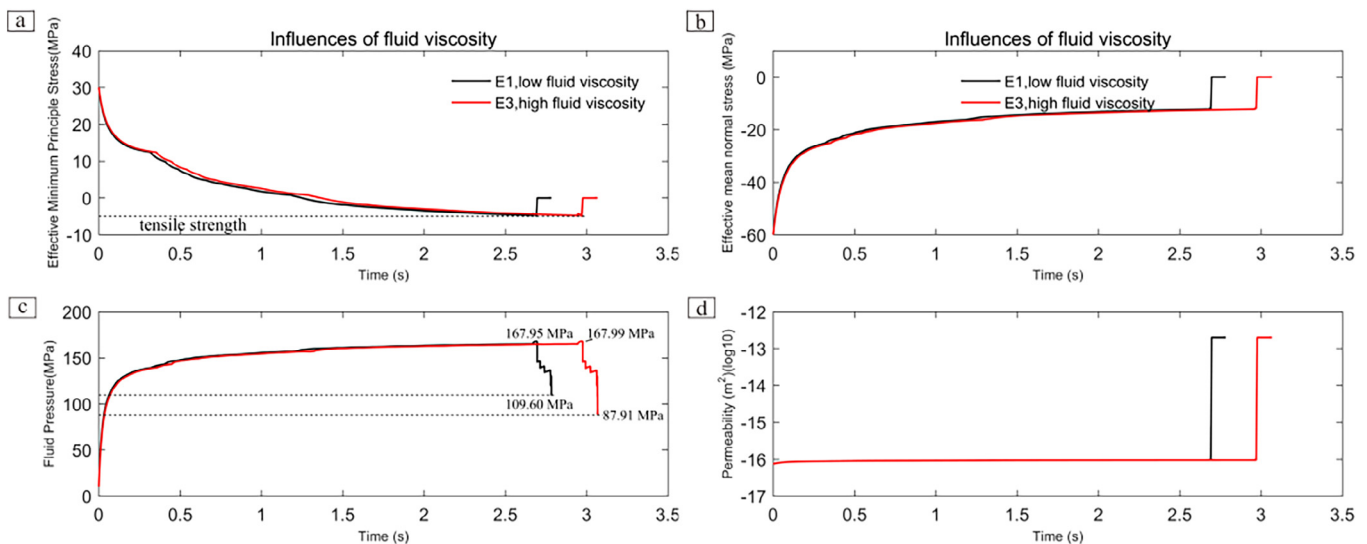

Fig. 9. The effective minimum principle stress (a), the effective mean normal stress (b), the fluid pressure (c), and the permeability (d) at the reference node against time in the first (E1) and third (E3) numerical experiments. The only different variable between E1 and E3 was fluid viscosity. The tensile strength of the reference node was satisfied later in E3 than that in E1.
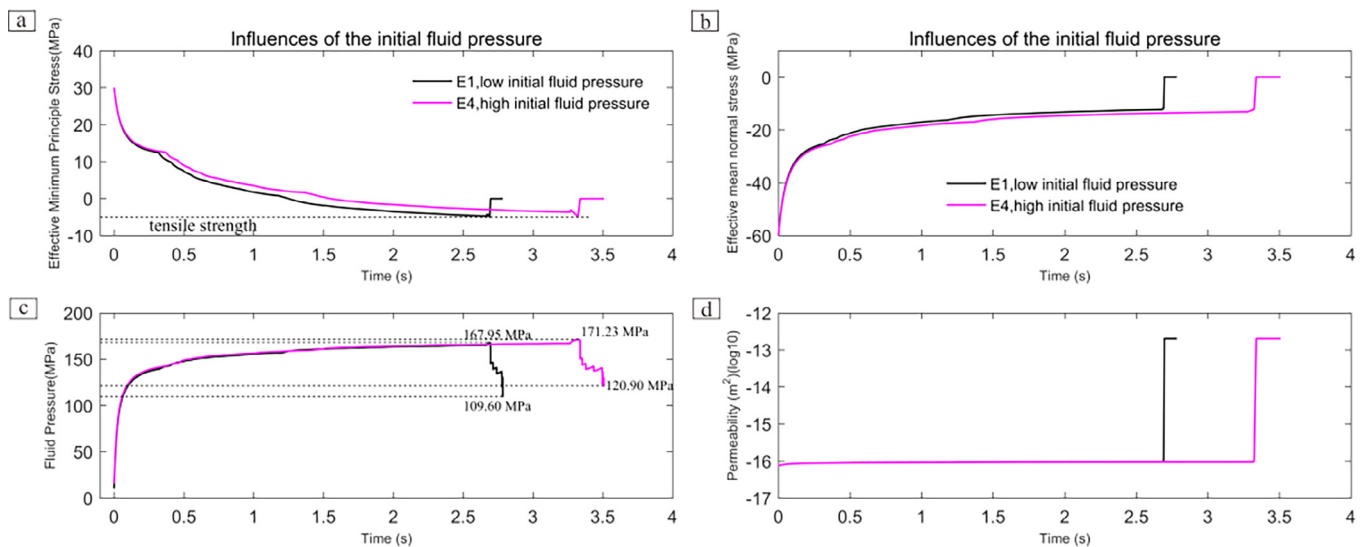
Fig. 10. The evolutions of the effective minimum principle stress (a), the effective mean normal stress (b), the fluid pressure (c), and the permeability (d) at the reference node in the first (E1) and fourth (E4) numerical experiments. The only different variable between E1 and E4 was the initial fluid pressure. The tensile strength of the reference node was satisfied later in E4 than that in E1.

solutions. Tungsten solubility increases with fluid pressure and the concentration of CO_2 in solutions and changes from 23 to 50 ppm.

The dominant iron species are $FeCl_2^0$, $FeCl^+$, and Fe^{2+}, the concentrations of which are 2–10 orders of magnitude higher than those of $FeOH^+$, FeO^0, and $HFeO_2^-$ (Fig. 14). The concentrations of $FeCl_2^0$, $FeCl^+$, Fe^{2+}, and $FeOH^+$ increase with fluid pressure, while those of FeO^0, and $HFeO_2^-$ decrease with fluid pressure.

Tungsten species are dominated by HWO_4^- and $NaWO_4^-$ and their concentrations are 1–2 orders of magnitude higher than those of $NaHWO_4^0$, $H_2WO_4^0$, and WO_4^{2-} (Fig. 14). The concentration of HWO_4^- is positively correlated to fluid pressure, while the concentration of $NaWO_4^-$ has a negative correlation to fluid pressure. The source data can be accessed from the supplementary table in the web version.

4.7. Chemical responses to hydraulic fracturing driven by CO_2-saturated fluids

Table 4 shows the change of pH and tungsten solubility in the first,

third, fourth, and the fifth numerical experiments. The fluid pressure fluctuated over ten times in each numerical experiment. pH in these four numerical experiments had a range of 3.42–3.91 and increased by 0.32 on average. The increase in pH resulted in an accumulated decrease of 12.61–16.25 ppm in tungsten solubility, which accounted for 31.05% of the maximum tungsten solubility on average.

5. Discussion

5.1. Validity of numerical experiments of hydraulic fracturing

Magmatic-hydrothermal fluids are highly compressible and have a significantly low viscosity compared to H_2O-bearing silicate melts (Audétat and Keppler, 2004). Previous studies have identified that fluid compressibility has an influence on seismic activities (e.g. Geli et al., 2014; Geli et al., 2016). Findings from the field of oil and gas industry suggest that an increase in fluid compressibility and fluid viscosity slows the change of the effective stresses and prolongs the time of
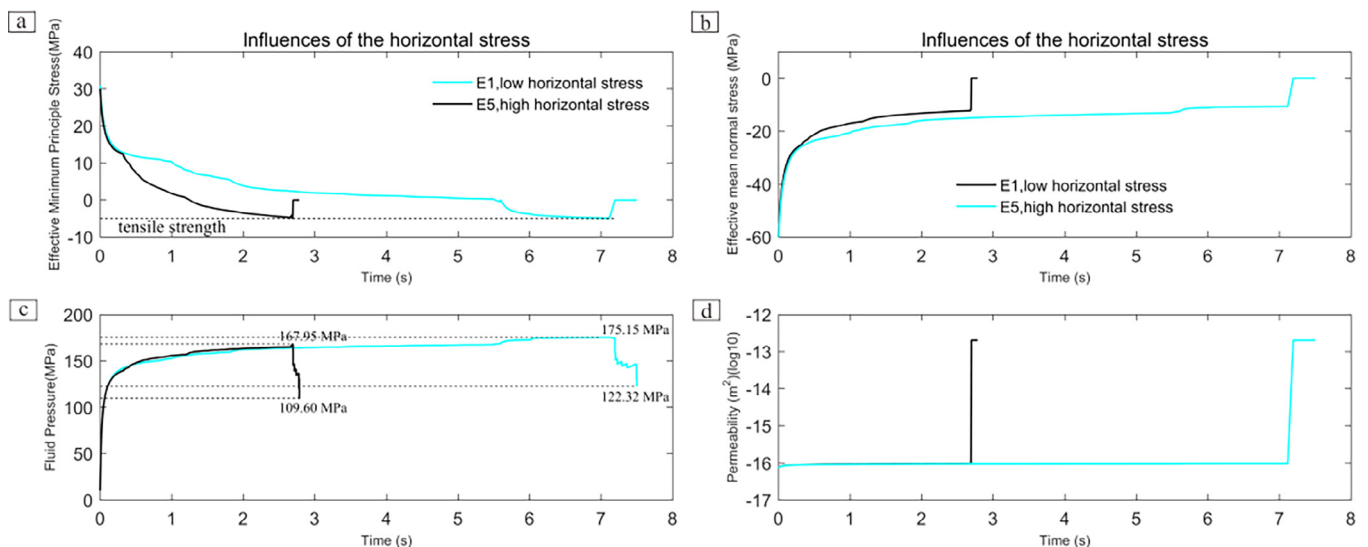

Fig. 11. The effective minimum principle stress (a), the effective mean normal stress (b), the fluid pressure (c), and the permeability (d) at the reference node against time in the first (E1) and fifth (E5) numerical experiments. The only different variable between E1 and E5 was the horizontal stress loaded in the first stage of the numerical experiments. The tensile strength of the reference node was satisfied later in E5 than that in E1.
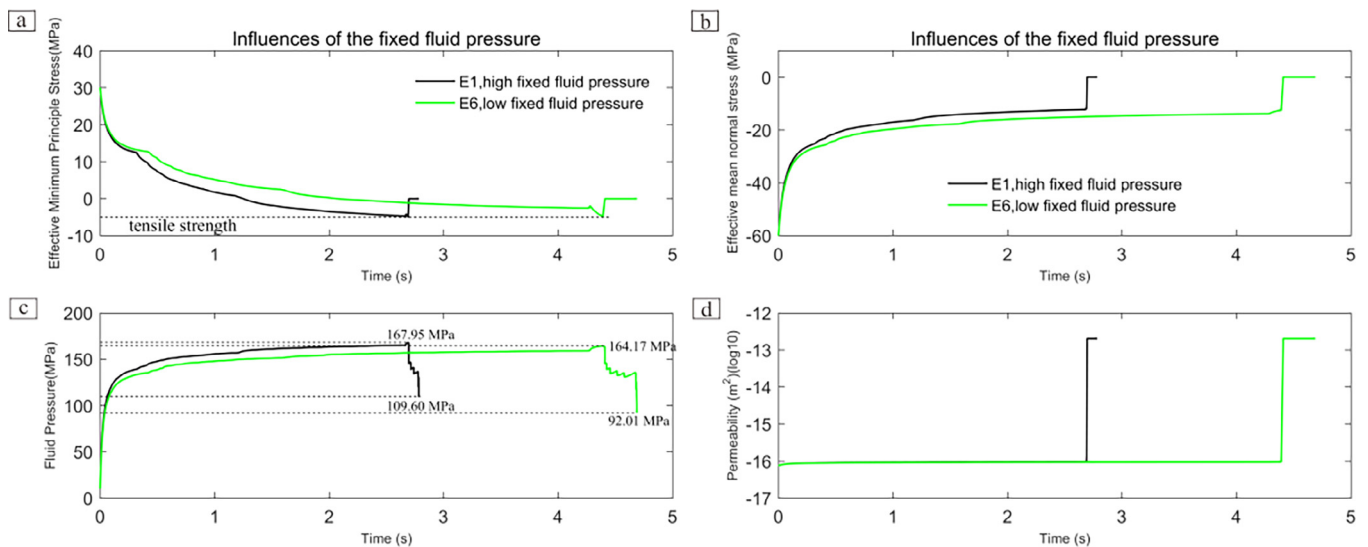
Fig. 12. The effective minimum principle stress (a), the effective mean normal stress (b), the fluid pressure (c), and the permeability (d) at the reference node against time in the first (E1) and sixth (E6) numerical experiments. The only different variable between E1 and E6 was the fixed fluid pressure loaded in the second stage of the numerical experiments. The tensile strength of the reference node was satisfied later in E6 than that in E1. The fluid pressure in E6 fluctuated from 164.2 MPa to 92.0 MPa.

fracturing (e.g. Chen et al., 2015; Ishida et al., 2004). This is consistent with our numerical experiments (E1, E2, and E3).

The classic equations for analyzing the breakdown pressure suggest that this parameter is positively correlated to the initial pore pressure and the minimum horizontal stress (cf. Bunger et al., 2010; Kumari et al., 2018). This is in accord with the results of the fourth and fifth numerical experiments.

The sixth numerical experiment (E6) had a lower fixed fluid pressure than the first one (E1). A low fixed fluid pressure caused a low pressurization rate (Fig. 12c). The breakdown pressure in E6 was lower than that in E1. Findings from laboratory and numerical experiments of hydraulic fracturing suggest that the breakdown pressure increases with the pressurization rate (e.g. Detournay and Cheng, 1992; Zhuang et al., 2018; Zoback et al., 1977). This is consistent with the difference of the breakdown pressure between E6 and E1.

Hydraulic fracturing in the numerical experiments was triggered at a time scale of a few seconds. The driving fluid pressure used in the numerical experiments is two times the lithostatic pressure at that depth. The fluid overpressure formed in crust often falls between the hydrostatic level and the lithostatic level at a given depth (Peacock et al., 2017). Comparisons between the first and sixth numerical

experiments indicate that a decrease in the driving fluid pressure prolongs the time of fracturing. Therefore, the timescales of hydraulic fracturing during formation of the tungsten deposits in southern China may be longer than those in the numerical experiments. Certainly, hydraulic fracturing is a transient mechanical process and its timescales are shorter than those of hydrothermal flow and chemical reactions in hydrothermal systems (Cox, 2005; Cox, 2016; Jébrak, 1997; Zhao et al., 2012). A typical example of this transient process is fluid-driven earthquakes (e.g. Miller et al., 2004).

5.2. Comparisons with other thermodynamic models and experimental results

pH in the numerical experiments of hydraulic fracturing is 3.42–3.91, which is lower than that (pH = 4–6) of the mineralizing fluids forming tungsten deposits (Wood and Samson, 2000). This difference may be caused by the assumption that CO_2 dissolved in NaCl solutions is saturated in the thermodynamic model. Note that the pH data in Wood and Samson (2000) come from the tungsten deposits in the world except China and no pH of the tungsten deposits of southern China is reported until now.
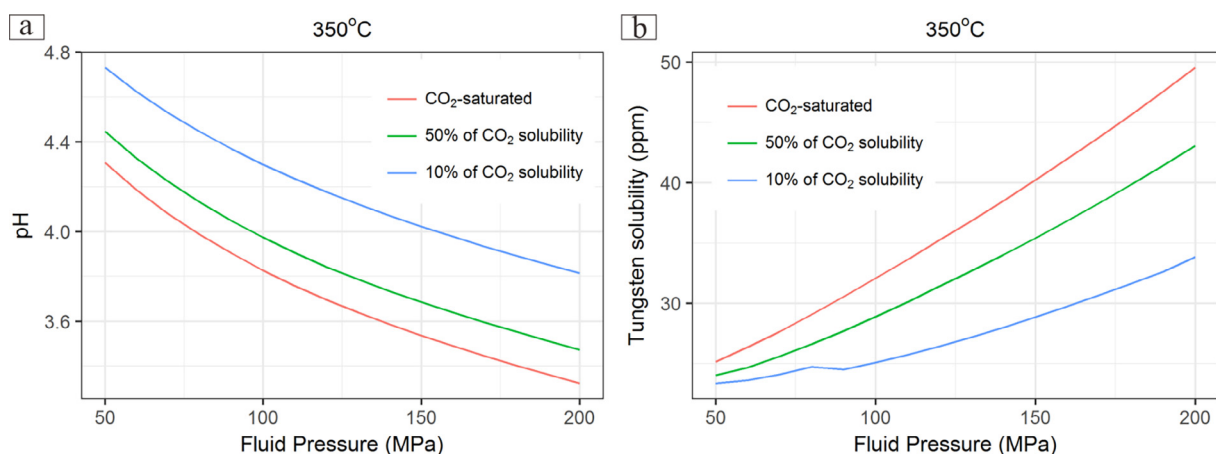

Fig. 13. The change of pH (a) and tungsten solubility (b) against fluid pressure under 350 °C and 10 w.t.% NaCl in the thermodynamic model Three lines represent three different CO_2 concentrations in NaCl aqueous solutions. pH decreases with fluid pressure and tungsten solubility increases with fluid pressure.
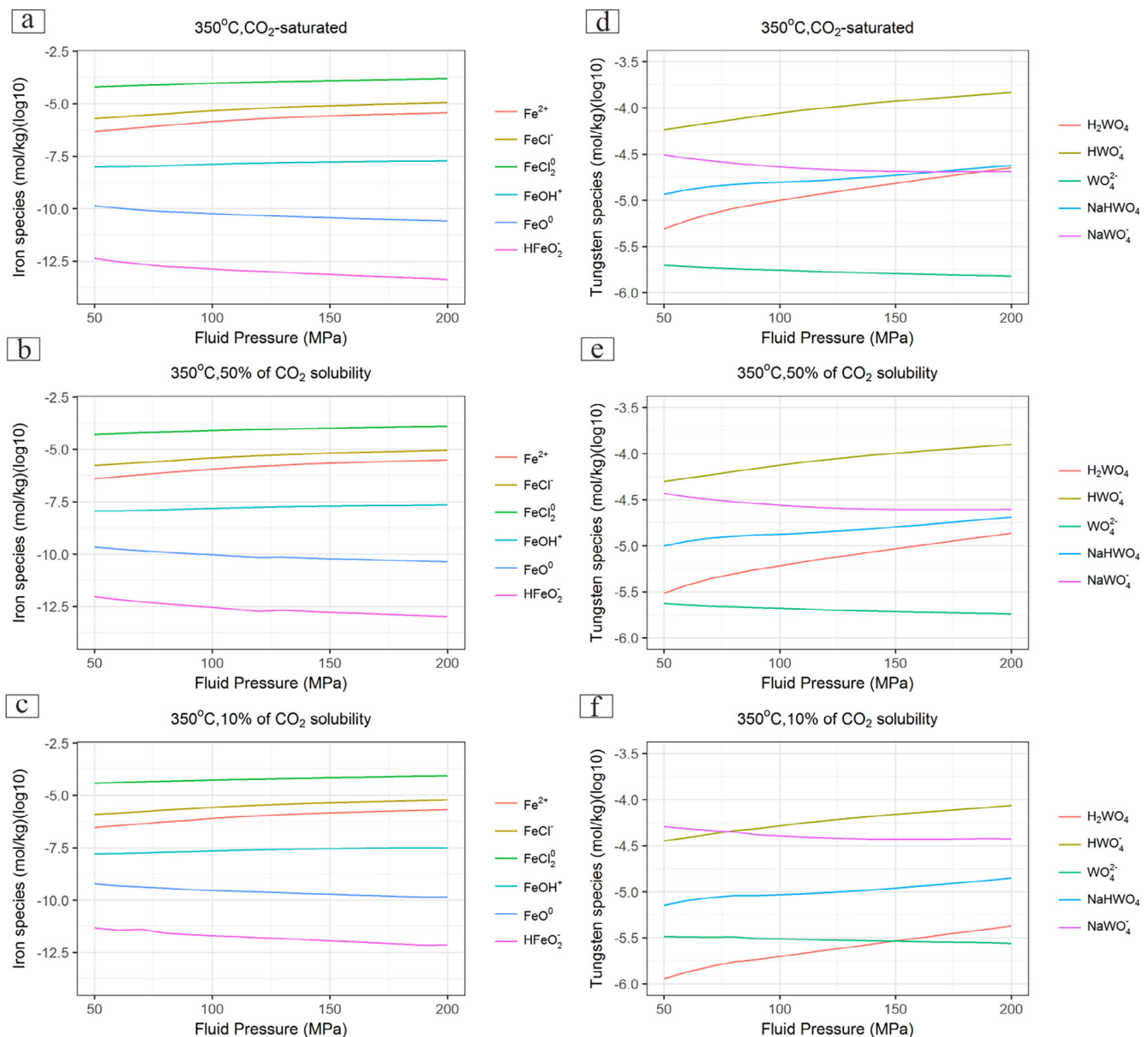
Fig. 14. The change of iron species and tungsten species against fluid pressure in NaCl solutions with different CO_2 concentrations. The dominant iron species and tungsten species are $FeCl_2^0$ and HWO_4^-, respectively.

Polya (1990) found from a thermodynamic model that tungsten solubility decreases with decreasing fluid pressure. The tungsten-bearing species in his model are HWO_4^- and WO_4^{2-}. More tungsten-bearing species were considered by Wood and Samson (2000). The dominant tungsten species in their models is HWO_4^-, which is consistent with our models. Tungsten solubility in their models reaches a few hundred ppm, which is higher than that in our models. This difference comes from that scheelite and Ca-related reactions are absent in our models. Their thermodynamic models suggest that tungsten solubility is not a monotonic function of fluid pressure. In contrast, tungsten solubility is positively correlated to fluid pressure in our models. The comparisons above indicate that the results strongly depend on the tungsten species and the existence of CO_2 in hydrothermal fluids.

Table 4

The change of pH and tungsten solubility in the numerical experiments of hydraulic fracturing.

	E1	E3	E4	E5	Average
Breakdown pressure (MPa)	167.95	167.99	171.23	175.15	–
pH range	[3.45, 3.76]	[3.45, 3.91]	[3.43, 3.69]	[3.42, 3.68]	–
pH increase in log unit	0.31	0.46	0.26	0.26	0.32
Fluctuation times	11	14	15	15	–
Maximum tungsten solubility (ppm)	43.41	43.42	44.01	44.73	–
Accumulated tungsten decrease (ppm)	12.61	16.25	12.79	12.82	13.62
$\frac{Accumulated\ tungsten\ decrease}{Maximum\ tungsten\ solubility}$	29.05%	37.42%	29.08%	28.66%	31.05%

Liu et al. (2017b) conducted crystallization experiments of wolframite in a hydrothermal diamond-anvil cell using [Fe,Mn]WO$_4$-LiCO$_3$-H$_2$O as starting materials. They found that solubility of wolframite increased with CO$_2$ component in solutions. Therefore, our thermodynamic results are consistent with their findings although Mn-related reactions are absent in our models.

5.3. Hydraulic fracturing and wolframite precipitation

The WO$_3$ grade in the vein-type tungsten deposits of southern China generally reach 0.15–1.5% (Mao et al., 2013), which are 10^4–10^5 times the Clarke value of 0.6 part per million for the crust in eastern China (Chi et al., 2012). However, it is poorly understood how the ores are efficiently precipitated from hydrothermal fluids (e.g. Liu et al., 2015; Polya, 1988). The similar question is also pending in other types of hydrothermal deposits (e.g. Heinrich et al., 2005; Henley and Berger, 2000; Zhao et al., 2017a).

The mineralizing fluids of the tungsten deposits are interpreted to have a magmatic source (e.g. Chen et al., 2018; Li et al., 2018). In this case, simple cooling is inefficient to precipitate minerals because rocks have a low thermal conductivity (Barton and Toulmin, 1961; Heinrich, 2005; Heinrich and Candela, 2014). Over ten fluctuations of fluid pressure were identified in our numerical experiments. The first fluctuation was caused by a significant increase in the permeability of the reference node. Repeated recovery of fluid pressure resulted in fracturing of the surrounding nodes and the following fluctuations of fluid pressure. The fluid pressure drops in our numerical experiments were smaller than that caused by a seismic slip (Weatherley and Henley, 2013). However, repeated fluctuations of fluid pressure during a hydraulic fracturing process still decreased the solubility of CO$_2$ and caused CO$_2$ escaping from hydrothermal fluids. CO$_2$ escaping increased pH and broke the chemical equilibrium where the dominant iron-bearing and tungsten-bearing species decreased. The accumulated tungsten precipitated after hydraulic fracturing reached 12.61–16.25 ppm, which accounted for approximately 30% of the maximum tungsten solubility in solutions. Therefore, hydraulic fracturing is an efficient process for precipitating wolframite in the tungsten deposits.

5.4. Limitations and further improvements

The numerical models in this study are established on many assumptions and provide an explanation for the mechanisms of precipitating wolframite from CO$_2$-saturated hydrothermal fluids. Further modifications are suggested for improving the models and better explaining how wolframite precipitates from hydrothermal fluids.

First, wolframite in the tungsten deposits in southern China is a solid solution between the two end-members, ferberite (FeWO4) and hüebnerite (MnWO4) (e.g. Wang and Ji, 1989; Xie et al., 2017). Thermodynamic data related to MnWO4 and Mn^{2+} are required for further improving the thermodynamic model of tungsten solubility in hydrothermal fluids.

Second, CO$_2$-bearing fluid inclusions are not identified in all the tungsten deposits (cf. Ni et al., 2015). However, it remains poorly understood how wolframite precipitates from CO$_2$-free hydrothermal solutions that are not mixed with meteoric fluids. This issue also met in other types of hydrothermal deposits (e.g. Heinrich et al., 2005). An attempt to solve this issue is to consider the concept of fluid mixing proposed by Lester et al. (2012) and examine whether and how chaotic advection of reactive hydrothermal fluids causes mineral deposition.

Third, fluid temperature was assumed to be independent on fluid pressure change in our models. Whether a decrease in fluid pressure causes a decrease in fluid temperature should be examined because

fluid temperature is a key variable controlling solubility of tungsten and other metals in hydrothermal fluids (Yardley, 2005). This question is related to adiabatic decompression (Heinrich et al., 2005), which is quantified by the Joule-Thompson coefficient (Stauffer et al., 2014). However, the Joule-Thompson coefficients of NaCl aqueous solutions over 300 °C and 100 MPa are unknown (Wood and Spera, 1984). Determination of this coefficient at higher temperatures and pressures may help us find the mechanisms precipitating wolframite and other ore minerals in magmatic-hydrothermal deposits.

6. Conclusions

Finite element based numerical experiments of hydraulic fracturing coupled with a multi-component thermodynamic model were conducted to examine whether the change of fluid pressure during a hydraulic fracturing process could cause wolframite precipitation. CO$_2$-bearing aqueous NaCl solutions with a salinity of 10 wt% at 350 °C were used in the models. Hydraulic fracturing in the numerical experiments is driven by fluids at a fixed fluid pressure. The changes of fluid pressure in the numerical experiments are linked to the thermodynamic model. The numerical experiments provide the following implications for the mechanisms precipitating wolframite in the tungsten deposits of southern China:

(1) Hydraulic fracturing is influenced by fluid compressibility, fluid viscosity, the initial fluid pressure, the horizontal stress, and the fixed fluid pressure. An increase in CO$_2$ concentration increases the fluid compressibility and prolongs the time of hydraulic fracturing. An increase in fluid viscosity, the initial fluid pressure, and the horizontal stress and a decrease in the fixed fluid pressure also lengthen the time of fracturing.

(2) CO$_2$ solubility in NaCl aqueous solutions is positively correlated to fluid pressure. A decrease in fluid pressure increases pH and reduces the concentrations of the dominant iron species and the dominant tungsten species. Therefore, tungsten solubility decreases with decreasing fluid pressure. The pH derived from the thermodynamic model is between 3.3 and 4.7 depending on fluid pressure and CO$_2$ concentrations. Tungsten solubility in fluids at 350 °C reaches tens of ppm.

(3) Over ten fluctuations of fluid pressure were identified during a hydraulic fracturing process. These fluid pressure fluctuations could cause a decrease in tungsten solubility by 12.61–16.25 ppm, which accounts for 31.05% of the maximum tungsten solubility. Thus, hydraulic fracturing is an efficient process for precipitating wolframite from CO$_2$-bearing hydrothermal fluids.

A. Appendix

Basic equations

Elastic-plastic finite deformation theory is used in PANDAS (Xing and Makinouchi, 2002).The rate of deformation tensor is supposed to be the sum of an elastic part D^e and a plastic part D^p:

$$D_{ij} = D_{ij}^e + D_{ij}^p \tag{A-1}$$

which are prescribed by the Hookes law and the associated flow rule, respectively. The elastic strain increment D_{ij}^e is:

$$D_{ij}^e = [C_{ijkl}^e]^{-1}\sigma_{kl}^o \tag{A-2}$$

in which σ_{kl}^o is the Jaumann derivative of σ_{kl}.

The associated flow rule is as follows:

$$D_{ij}^p = \dot{\lambda}\frac{\partial f}{\partial \sigma_{ij}} \tag{A-3}$$

in which $\dot{\lambda}$ is the plastic multiplier, σ_{ij} is the Cauchy stress, and f is a plastic potential. Both the Maximum Tensile Stress Criterion and the Mohr-Coulomb Criterion are applied here.

The effective stress σ_{ij}' is used when fluids are filled in the pores:

$$\sigma_{ij}' = \sigma_{ij} - \alpha P \delta_{ij} \tag{A-4}$$

in which P is the pore fluid pressure, α is the coefficient of the pore pressure, and δ_{ij} is the Kronecker delta.

Following the mass conversation theory, the pressure diffusion equation is:

$$k\nabla^2 P = \frac{1}{Q}\frac{\partial P}{\partial t} - a\frac{\partial \varepsilon_v}{\partial t} \tag{A-5}$$

$$\frac{1}{Q} = \mu S \tag{A-6}$$

$$S = \frac{1}{K_s} + \frac{\phi}{K_f} \tag{A-7}$$

in which k is the permeability scalar, Q is the Biot constant, $\varepsilon_v = \varepsilon_{11} + \varepsilon_{22} + \varepsilon_{33}$ is the volume strain, μ is the fluid viscosity, ϕ is the porosity, K_f is the bulk modulus of the fluid and equals the reciprocal of fluid compressibility, and K_s is the bulk modulus of the solid matrix.

The permeability scalar follows the exponential law of effective stress (David et al., 1994):

$$k = \xi k_0 exp\left(-\omega\left(\frac{\sigma_{kk}}{3} - \alpha P\right)\right) \tag{A-8}$$

$$\frac{k}{k_0} = \left(\frac{\phi}{\phi_0}\right)^3 \tag{A-9}$$

in which k_0 is the initial permeability scalar, ϕ_0 is the initial porosity, ω is the effective pressure sensitivity coefficient, $\frac{\sigma_{kk}}{3} - \alpha P$ is the effective mean normal stress, and ξ is a damage factor. $\xi = 1$ when the rock is in elastic state. Low-porosity crystalline rocks have an effective pressure sensitivity coefficient of 10^{-3}–10^{-2} MPa^{-1} (David et al., 1994). $\omega = 5 \times 10^{-3}$ MPa^{-1} was used in our models. Findings from laboratory and field experiments of hydraulic fracturing suggest that the rock permeability is increased by at least 10^2–10^3 times after fracturing (e.g. Evans et al., 2012; Ladner and Häring, 2009; Watanabe et al., 2017). In our models, $\xi = 2000$ is used when one of the two criterions above is met.

Appendix B. Supplementary data

Supplementary data associated with this article can be found, in the online version, at https://doi.org/10.1016/j.oregeorev.2018.08.027.

References

Audétat, A., Günther, D., Heinrich, C.A., 1998. Formation of a magmatic-hydrothermal ore deposit: insights with LA-ICP-MS analysis of fluid inclusions. Science 279 (5359), 2091–2094.

Audétat, A., Keppler, H., 2004. Viscosity of fluids in subduction zones. Science 303 (5657), 513–516.

Baker, T., 2002. Emplacement depth and carbon dioxide-rich fluid inclusions in intrusion-related gold deposits. Econ. Geol. 97 (5), 1111–1117.

Bando, S., Takemura, F., Nishio, M., Hihara, E., Akai, M., 2004. Viscosity of aqueous NaCl solutions with dissolved CO2 at (30 to 60) C and (10 to 20) MPa. J. Chem. Eng. Data 49 (5), 1328–1332.

Barnhoorn, A., Cox, S.F., Robinson, D.J., Senden, T., 2010. Stress- and fluid-driven failure during fracture array growth: implications for coupled deformation and fluid flow in the crust. Geology 38 (9), 779–782.

Barton, P., Toulmin, P., 1961. Some mechanisms for cooling hydrothermal fluids. US Geological Survey Professional Paper 424, 348–352.

Beach, A., 1980. Numerical models of hydraulic fracturing and the interpretation of syntectonic veins. J. Struct. Geol. 2 (4), 425–438.

Bons, P.D., 2001. The formation of large quartz veins by rapid ascent of fluids in mobile hydrofractures. Tectonophysics 336, 1–17.

Bunger, A., Lakirouhani, A., Detournay, E., 2010. Modelling the effect of injection system compressibility and viscous fluid flow on hydraulic fracture breakdown pressure, Rock Stress and Earthquakes-Proceedings of the 5th International Symposium on In-Situ Rock Stress, pp. 59-67.

Černý, P., Blevin, P.L., Cuney, M., London, D., 2005. Granite-Related Ore Deposits. Society of Economic Geologists 100th Anniversary: 337-370.

Chen, L.-L., Ni, P., Li, W.-S., Ding, J.-Y., Pan, J.-Y., Wang, G.-G., Yang, Y.-L., 2018. The link between fluid evolution and vertical zonation at the Maoping tungsten deposit, Southern Jiangxi, China: fluid inclusion and stable isotope evidence. J. Geochem. Explor. 192, 18–32.

Chen, L., Tian, S., Li, G., Wan, X., 2015. Initiation pressure models for supercritical CO2 fracturing and sensitivity analysis. Rock Soil Mech. 36 (2), 125–131 (in Chinese with English Abstract).

Chen, Y.C., Pei, R.F., Zhang, H.L., Lin, X.D., Li, C.Y., Hu, Y.J., Liu, H.Q., Xian, B.Q., 1989.

The Geology of Nonferrous and Rare Metal Deposits Related to Mesozoic Granitoids in Nanling Region. Geological Publishing Housing, Beijing, China, pp. 507.

Chi, Q.H., Wang, X.Q., Xu, S.F., Zhou, J., Liu, H.L., Liu, D.S., Zhang, B.M., Wang, W., 2012. Temporal and spatial distribution of tungsten and tin in South China Continent. Earth Sci. Front. 19 (3), 70–83 (In Chinese with English abstract).

Cosgrove, J., 1995. The expression of hydraulic fracturing in rocks and sediments. Special Publication-Geological Society of London 92 187 187.

Cosgrove, J.W., 2001. Hydraulic fracturing during the formation and deformation of a basin: a factor in the dewatering of low-permeability sediments. AAPG Bull. 85 (4), 737–748.

Cox, S.F., 2005. Coupling between deformation, fluid pressures, and fluid flow in ore-producing hydrothermal systems at depth in the crust. In: Hedenquist, J.W., Thompson, J.F.H., Goldfarb, R.J., Richards, J.P. (Eds.), Economic Geology One Hundredth Anniversary Volume. Society of Economic Geologists, Litteton, Colorado, pp. 39–76.

Cox, S.F., 2007. Structural and isotopic constraints on fluid flow regimes and fluid pathways during upper crustal deformation: an example from the Taemas area of the Lachlan Orogen, SE Australia. J. Geophys. Res.: Solid Earth 112 (B8), B08208.

Cox, S.F., 2010. The application of failure mode diagrams for exploring the roles of fluid pressure and stress states in controlling styles of fracture-controlled permeability enhancement in faults and shear zones. Geofluids 10 (1–2), 217–233.

Cox, S.F., 2016. Injection-driven swarm seismicity and permeability enhancement: implications for the dynamics of hydrothermal ore systems in high fluid-flux, over-pressured faulting regimes—an invited paper. Econ. Geol. 111 (3), 559–587.

David, C., Wong, T.F., Zhu, W., Zhang, J., 1994. Laboratory measurement of compaction-induced permeability change in porous rocks: implications for the generation and maintenance of pore pressure excess in the crust. Pure Appl. Geophys. 143 (1–3), 425–456.

Detournay, E., Cheng, A., 1992. Influence of pressurization rate on the magnitude of the breakdown pressure. The 33th U.S. Symposium on Rock Mechanics (USRMS). American Rock Mechanics Association, Santa Fe, New Mexico.

Dick, J., 2017. CHNOSZ: Thermodynamic Calculations for Geobiochemistry, https://CRAN.R-project.org/package=CHNOSZ.

Drummond, S.E., 1981. Boiling and Mixing of Hydrothermal Fluids: Chemical Effects on Mineral Precipitation (Ph.D. thesis). Pennsylvania State University.

Dubacq, B., Bickle, M.J., Evans, K.A., 2013. An activity model for phase equilibria in the H2O–CO2–NaCl system. Geochim. Cosmochim. Acta 110, 229–252.

Evans, K.F., Zappone, A., Kraft, T., Deichmann, N., Moia, F., 2012. A survey of the induced seismic responses to fluid injection in geothermal and CO2 reservoirs in Europe. Geothermics 41, 30–54.

Fang, G., Chen, Z., Chen, Y., Li, J., Zhao, B., Zhou, X., Zeng, Z., Zhang, Y., 2015. Geophysical investigations of the geology and structure of the Pangushan-Tieshanlong tungsten ore field, South Jiangxi, China—Evidence for site-selection of the 2000-m Nanling Scientific Drilling Project (SP-NLSD-2). J. Asian Earth Sci. 110, 10–18.

Fekete, S.W., Philipp, Driesner, T., Bouvier, A.-S., Baumgartner, L., Heinrich, C.A., 2016. Contrasting hydrological processes of meteoric water incursion during magmatic–hydrothermal ore deposition: an oxygen isotope study by ion microprobe. Earth Planet. Sci. Lett. 451, 263–271.

Fleury, M., Deschamps, H., 2009. Viscosity and electrical conductivity of aqueous NaCl solutions with dissolved CO2. Energy Procedia 1 (1), 3129–3133.

Geli, L., Piau, J.-M., Dziak, R., Maury, V., Fitzenz, D., Coutellier, Q., Henry, P., Broseta, D., Steele-MacInnis, M., Driesner, T., 2014. Seismic precursors linked to highly compressible fluids at oceanic transform faults. Nat. Geosci.

Geli, L., Piau, J.-M., Maury, V., Fitzenz, D., Dziak, R., Coutellier, Q., Henry, P., Broseta, D., Steele-MacInnis, M., Driesner, T., 2016. Corrigendum: seismic precursors linked to highly compressible fluids at oceanic transform faults. Nat. Geosci. 9 (1) 83 83.

Gercek, H., 2007. Poisson's ratio values for rocks. Int. J. Rock Mech. Min. Sci. 44 (1), 1–13.

Gerdes, M.L., Baumgartner, L.P., Person, M., 1998. Convective fluid flow through heterogeneous country rocks during contact metamorphism. J. Geophys. Res.: Solid Earth 103 (B10), 23983–24003.

Gibert, F., Moine, B., Schott, J., Dandurand, J.-L., 1992. Modeling of the transport and deposition of tungsten in the scheelite-bearing calc-silicate gneisses of the Montagne Noire, France. Contrib. Mineral. Petrol. 112 (2–3), 371–384.

Gong, X., Yan, G., Ye, T., Zhu, X., Li, Y., Zhang, Z., Jia, W., Yao, X., 2015. A study of ore-forming fluids in the Shimensi tungsten deposit, Dahutang tungsten polymetallic ore field, Jiangxi Province, China. Acta Geol. Sin.-Engl. Ed. 89 (3), 822–835.

Gu, J.Y., 1984. Morpholgical zonation of tungsten deposits in South China. In: Yu, H.Z. (Ed.), Proceedings of Symposium on Tungsten Geology (Chinese edition). Geological Publishing House, Nanchang, pp. 35–45.

Han, L., Huang, X., Jie, L., Pengli, H., Junming, Y., 2016. Oxygen fugacity variation recorded in apatite of the granite in the Dahutang tungsten deposit, Jiangxi Province, South China. Acta Petrol. Sin. 32 (3), 746–758.

Hanson, R.B., 1995. The hydrodynamics of contact metamorphism. Geol. Soc. Am. Bull. 107 (5), 595–611.

Harlaux, M., Mercadier, J., Marignac, C., Peiffert, C., Cloquet, C., Cuney, M., 2018. Tracing metal sources in peribatholitic hydrothermal W deposits based on the chemical composition of wolframite: the example of the Variscan French Massif Central. Chem. Geol. 479, 58–85.

He, S., Xi, X., 1988. The genesis of the en-echelon structure of tungsten veins in Xihuashan, Jiangxi. Acta Geol. Sin.-Chin. Ed. 1 (1), 31–42.

Heinrich, C., 2005. The physical and chemical evolution of low-salinity magmatic fluids at the porphyry to epithermal transition: a thermodynamic study. Mineral. Deposita 39 (8), 864–889.

Heinrich, C.A., 1990. The chemistry of hydrothermal tin(-tungsten) ore deposition. Econ.

Geol. 85 (3), 457–481.

Heinrich, C.A., Seward, T.M., 1990. A spectrophotometric study of aqueous iron (II) chloride complexing from 25 to 200°C. Geochim. Cosmochim. Acta 54 (8), 2207–2221.

Heinrich, C.A., Halter, W., Landtwing, M.R., Pettke, T., 2005. The formation of economic porphyry copper (-gold) deposits: constraints from microanalysis of fluid and melt inclusions. Geological Society, London, Special Publications 248 (1), 247–263.

Heinrich, C.A., 2007. Fluid-fluid interactions in magmatic-hydrothermal ore formation. Rev. Mineral. Geochem. 65 (1), 363–387.

Heinrich, C.A., Candela, P.A., 2014. 13.1 – fluids and ore formation in the Earth's crust. In: Turekian, H.D.H.K. (Ed.), Treatise on Geochemistry (Second Edition). Elsevier, Oxford, pp. 1–28.

Helgeson, H.C., 1969. Thermodynamics of hydrothermal systems at elevated temperatures and pressures. Am. J. Sci. 267 (7), 729–804.

Helgeson, H.C., Kirkham, D.H., Flowers, G.C., 1981. Theoretical prediction of the thermodynamic behavior of aqueous electrolytes by high pressures and temperatures; IV, Calculation of activity coefficients, osmotic coefficients, and apparent molal and standard and relative partial molal properties to 600 degrees C and 5kb. Am. J. Sci. 281, 1249–1516.

Henley, R.W., Berger, B.R., 2000. Self-ordering and complexity in epizonal mineral deposits. Annu. Rev. Earth Planet. Sci. 28, 669–719.

Holloway, J.R., 1976. Fluids in the evolution of granitic magmas: consequences of finite CO2 solubility. Geol. Soc. Am. Bull. 87 (87), 1513.

Huang, H., Chang, H., Fu, J., Wang, X., Li, T., 2006. Formation pressure of wolframite_vein deposits and emplacement depth of related granite in Xihuashan, Jiangxi Province. Mineral Deposits 25 (5), 562–571 (In Chinese with English Abstract).

Huang, H.L., Chang, H.L., Li, F., Tan, J., Zhang, C.H., Zhou, Y., Yang, K., Yan, F., 2013. Microthermometry and characteristic element determination for the fluid inclusions in the wolframite and quartz in the drusy cavities of Xihuanshan tungsten deposit. Earth Sci. Front. 20 (2), 205–212.

Huang, L.-C., Jiang, S.-Y., 2014. Highly fractionated S-type granites from the giant Dahutang tungsten deposit in Jiangnan Orogen, Southeast China: geochronology, petrogenesis and their relationship with W-mineralization. Lithos 202, 207–226.

Ishida, T., Chen, Q., Mizuta, Y., Roegiers, J.-C., 2004. Influence of fluid viscosity on the hydraulic fracturing mechanism. J. Energy Resourc. Technol. 126 (3), 190–200.

Islam, A.W., Carlson, E.S., 2012. Viscosity Models and Effects of Dissolved CO2. Energy Fuel. 26 (8), 5330–5336.

Jébrak, M., 1997. Hydrothermal breccias in vein-type ore deposits: a review of mechanisms, morphology and size distribution. Ore Geol. Rev. 12 (3), 111–134.

Jiang, G.H., Hu, R.Z., Xie, G.Q., Zhao, J.H., Tang, Q.L., 2004. K-Ar ages of plutonism and mineralization at the Dajishan tungsten deposit, Jiangxi Province, China. Acta Mineral. Sin. 24 (3), 253–256 (In Chinese with English abstract).

Klyukin, Y.I., Lowell, R.P., Bodnar, R.J., 2017. A revised empirical model to calculate the dynamic viscosity of H2O-NaCl fluids at elevated temperatures and pressures (≤1000 °C, ≤500 MPa, 0–100 wt % NaCl). Fluid Phase Equilibria 433 (Supplement C), 193–205.

Korges, M., Weis, P., Lüders, V., Laurent, O., 2017. Depressurization and boiling of a single magmatic fluid as a mechanism for tin-tungsten deposit formation. Geology. https://doi.org/10.1130/G39601.1.

Kumagai, A., Yokoyama, C., 1999. Viscosities of aqueous NaCl solutions containing CO2 at high pressures. J. Chem. Eng. Data 44 (2), 227–229.

Kumari, W.G.P., Ranjith, P.G., Perera, M.S.A., Li, X., Li, L.H., Chen, B.K., Isaka, B.L.A., De Silva, V.R.S., 2018. Hydraulic fracturing under high temperature and pressure conditions with micro CT applications: geothermal energy from hot dry rocks. Fuel 230, 138–154.

Ladner, F., Häring, M.O., 2009. Hydraulic characteristics of the basel 1 enhanced geothermal system. Geotherm. Resourc. Council Trans. 33, 199–203.

Lecumberri-Sanchez, P., Vieira, R., Heinrich, C.A., Pinto, F., Wälle, M., 2017. Fluid-rock interaction is decisive for the formation of tungsten deposits. Geology.

Legros, H., Marignac, C., Tabary, T., Mercadier, J., Richard, A., Cuney, M., Wang, R.C., Charles, N., Lespinasse, M.Y., 2018. The ore-forming magmatic-hydrothermal system of the Piaotang W-Sn deposit (Jiangxi, China) as seen from Li-mica geochemistry. Am. Mineral. 103, 39–54.

Lester, D.R., Ord, A., Hobbs, B.E., 2012. The mechanics of hydrothermal systems: II. Fluid mixing and chemical reactions. Ore Geol. Rev. 49, 45–71.

Li, Q., Xing, H., 2015. Numerical analysis of the material parameter effects on the initiation of hydraulic fracture in a near wellbore region. J. Nat. Gas Sci. Eng. 27 (Part 3), 1597–1608.

Li, W.-S., Ni, Pei, Pan, Jun-Yi, Wang, G.-G., Chen, L.-L., Yang, Y.-L., Ding, J.-Y., 2018. Fluid inclusion characteristics as an indicator for tungsten mineralization in the Mesozoic Yaogangxian tungsten deposit, central Nanling district, South China. J. Geochem. Explor. 192, 1–17.

Li, Y.D., 1993. Poly-type model for tungsten deposits and vertical structural zoning model for vein-type tungsten deposits in south China. In: Kirkham, R.V., Sinclair, W.D., Thorpe, R.I., Duke, J.M. (Eds.), Mineral deposit modeling. Geological Association of Canada, Special Paper 40, pp. 555–568.

Liu, J., Mao, J., Ye, H., Zhang, W., 2011. Geology, geochemistry and age of the Hukeng tungsten deposit, Southern China. Ore Geol. Rev. 43 (1), 50–61.

Liu, X., Xing, H., Zhang, D., 2014. Fluid focusing and its link to vertical morphological zonation at the Dajishan vein-type tungsten deposit, South China. Ore Geol. Rev. 62 (1), 245–258.

Liu, X., Xing, H., Zhang, D., 2015. The mechanisms of the infill textures and its implications for the five-floor zonation at the Dajishan vein-type tungsten deposit, China. Ore Geol. Rev. 65 (Part 1), 365–374.

Liu, X., Xing, H., Zhang, D., 2017a. Influences of hydraulic fracturing on fluid flow and

mineralization at the vein-type tungsten deposits in southern China. Geofluids 2017, 11.

Liu, Y., Li, J., Zhao, Z., 2017b. A preliminary experimental study of the crystallization of wolframtie using hydrothermal diamond anvil cell. Earth Sci. Front. 24 (5), 159–166 (In Chinese with English Abstract).

Liu, Y.J., Ma, D.S., 1993. Vein-type tungsten deposits of China and adjoining regions. Ore Geol. Rev. 8, 233–246.

Lockner, D.A., 1995. Rock failure. Rock Physics & Phase Relations: A Handbook of Physical Constants, pp. 127–147.

Manning, C.E., Ingebritsen, S.E., 1999. Permeability of the continental crust: implications of geothermal data and metamorphic systems. Rev. Geophys. 37 (1), 127–150.

Manning, C.E., Shock, E.L., Sverjensky, D.A., 2013. The chemistry of carbon in aqueous fluids at crustal and upper-mantle conditions: experimental and theoretical constraints. Rev. Mineral. Geochem. 75 (1), 109–148.

Mao, J., Yanbo, C., Maohong, C., Pirajno, F., 2013. Major types and time–space distribution of Mesozoic ore deposits in South China and their geodynamic settings. Mineral. Deposita 48 (3), 267–294.

Mao, S., Hu, J., Zhang, Y., Lü, M., 2015. A predictive model for the PVTx properties of CO_2–H_2O–NaCl fluid mixture up to high temperature and high pressure. Appl. Geochem. 54, 54–64.

Mikucki, E.J., 1998. Hydrothermal transport and depositional processes in Archean lode-gold systems: a review. Ore Geol. Rev. 13 (1), 307–321.

Miller, S.A., Cristiano, C., Lauro, C., Massimo, C., Barchi, M., Kaus, B.J.P., 2004. Aftershocks driven by a high-pressure CO_2 source at depth. Nature 427 (6976), 724–727.

Mu, Z.G., Huang, F.S., Chen, C.Y., 1981. Oxygen, hydrogen and carbon isotope studies of Piantang and Xihuasha quartz vein-type tungsten deposits, Jiangxi Province. In: Yu, H.Z. (Ed.), Symposium on Tungsten Geology. Geological Publishing House, Nanchang, pp. 153–168.

Ni, P., Wang, X.D., Wang, G.G., Huang, J.B., Pan, J.Y., Wang, T.G., 2015. An infrared microthermometric study of fluid inclusions in coexisting quartz and wolframite from Late Mesozoic tungsten deposits in the Gannan metallogenic belt, South China. Ore Geol. Rev. 65 (Part 4), 1062–1077.

Nighswander, J.A., Kalogerakis, N., Mehrotra, A.K., 1989. Solubilities of carbon dioxide in water and 1 wt. % sodium chloride solution at pressures up to 10 MPa and temperatures from 80 to 200.degree.C. J. Chem. Eng. Data 34 (3), 355–360.

Pačevski, A., Götzinger, M., Dimitrijević, R., Cvetković, L., 2007. Oscillatory zoning in wolframite from Osanica, near Bor, Serbia. Neues Jahrbuch für Mineralogie - Abhandlungen 184 (2), 151–160.

Pariseau, W.G., 2006. Design analysis in Rock Mechanics. Taylor & Francis, London, pp. 560.

Peacock, D.C.P., Anderson, M.W., Rotevatn, A., Sanderson, D.J., Tavarnelli, E., 2017. The interdisciplinary use of "overpressure". J. Volcanol. Geotherm. Res.

Plimer, I.R., 1987. Fundamental parameters for the formation of granite-related tin deposits. Geol. Rundsch. 76 (1), 23–40.

Polya, D.A., 1988. Efficiency of hydrothermal ore formation and the Panasqueira W-Cu (Ag)-Sn vein deposit. Nature 333 (6176), 838–841.

Polya, D.A., 1990. Pressure- Independence of Wolframite solubility for Hydrothermal Vein Formation. Trans. Inst. Min. Metel. 99 (B59), 120–124.

Redkin, A.F., Kostromin, N.P., 2010. On the problem of transport species of tungsten by hydrothermal solutions. Geochem. Int. 48 (10), 988–998.

Robie, R.A., Hemingway, B.S., 1995. Thermodynamic properties of minerals and related substances at 298.15 K and 1 bar (10^5 pascals) pressure and at higher temperatures. Bulletin 2131, 461.

Rusk, B.G., Reed, M.H., Dilles, J.H., Klemm, L.M., Heinrich, C.A., 2004. Compositions of magmatic hydrothermal fluids determined by LA-ICP-MS of fluid inclusions from the porphyry copper–molybdenum deposit at Butte, MT. Chem. Geol. 210 (1–4), 173–199.

Rutqvist, J., Rinaldi, A.P., Cappa, F., Moridis, G.J., 2013. Modeling of fault reactivation and induced seismicity during hydraulic fracturing of shale-gas reservoirs. J. Pet. Sci. Eng. 107, 31–44.

Sakamoto, M., 1985. Internal structures and compositional variation of wolframite in the Takatori mine. Min. Geol. 35 (193), 317–329.

Seward, T.M., 1997. Metal transport by hydrothermal ore fluids. Geochem. Hydrotherm. Ore Depos. 435–486.

Shan, F., 1976. The geological characteristics of the Piaotang tungsten-tin deposit. Acta Geol. Sin.-Chin. Ed. 1, 1–16.

Sibson, R.H., 2004. Controls on maximum fluid overpressure defining conditions for mesozonal mineralisation. J. Struct. Geol. 26 (6–7), 1127–1136.

Soetaert, K., 2016. rootSolve: Nonlinear Root Finding, Equilibrium and Steady-State Analysis of Ordinary Differential Equations, https://CRAN.R-project.org/package= rootSolve.

Spycher, N., Pruess, K., 2005. CO2-H2O mixtures in the geological sequestration of CO2. II. Partitioning in chloride brines at 12–100°C and up to 600 bar. Geochim. Cosmochim. Acta 69 (13), 3309–3320.

Stauffer, P., Lewis, K.C., Stein, J., Travis, B., Lichtner, P., Zyvoloski, G., 2014. Joule-Thomson effects on the flow of liquid water. Transp. Porous Media 105 (3), 471–485.

Tindle, A.G., Webb, P.C., 1989. Niobian wolframite from Glen Gairn in the Eastern Highlands of Scotland: a microprobe investigation. Geochim. Cosmochim. Acta 53 (8), 1921–1935.

Tsuchiya, N., Yamada, R., Uno, M., 2016. Supercritical geothermal reservoir revealed by a granite–porphyry system. Geothermics 63, 182–194.

Walther, J.V., 1997. Determination of activity coefficients of neutral species in supercritical H2O solutions. Geochim. Cosmochim. Acta 61 (16), 3311–3318.

Wang, H.F., 2000. Theory of linear poroelasticity. Princeton Series in Geophysics. Princeton University Press, Princeton, pp. 287.

Wang, J.C., Wei, L.M., Zhu, W.F., Wan, F.L., Mo, Z.M., 2008. Texture and tectonic style of five storeyed type for the tungsten deposits in the Nanling Mountains, Southern China. Acta Geol. Sin.-Chin. Ed. 82 (7), 894–899.

Wang, Q., Hu, R., Peng, J., Bi, X., Wu, L., Liu, H., Su, B., 2007. Characteristics and significance of the fluid inclusions from Yaogangxian tungsten deposit in south of Hunan. Acta Petrol. Sin. 23 (9), 2263–2273 (in Chinese with English abstract).

Wang, X., Ren, M., Chen, J., 2017. The muscovite granites: parental rocks to the Nanling Range tungsten mineralization in South China. Ore Geol. Rev. 88, 702–717.

Wang, X.D., Ni, P., Zhang, B.S., Wang, T.G., 2012. Fluid inclusion studies of the Pangushan quartz-vein type tungsten deposit in southern Jiangxi Province. Acta Petrol. Et Mineral. 29 (5), 539–550 (In Chinese with English Abstract).

Wang, X.D., Ni, P., Yuan, S.D., Wu, S.H., 2013a. Fluid inclusion studies on coexisting cassiterite and quartz from the Piaotang tungsten deposit, Jiangxi Province, China. Acta Geol. Sin.-Chin. Ed. 87 (6), 850–859.

Wang, X.D., Ni, P., Yuan, S.D., Wu, S.H., 2013b. Fluid inclusion studies of Dajishan tungsten deposit in Jiangxi Province. Mineral Deposits 32, 308–322.

Wang, Y., Ji, S., 1989. X-ray powder diffraction investigation of the wolframite isomrphous series. Acta Mineral. Sin. 9 (3), 245–252 (In Chinese With English Abstract).

Watanabe, N., Egawa, M., Sakaguchi, K., Ishibashi, T., Tsuchiya, N., 2017. Hydraulic fracturing and permeability enhancement in granite from subcritical/brittle to supercritical/ductile conditions. Geophys. Res. Lett. 44 (11), 5468–5475.

Weatherley, D.K., Henley, R.W., 2013. Flash vaporization during earthquakes evidenced by gold deposits. Nat. Geosci. 6 (4), 294–298.

Wei, A., Wang, J., Mo, Z., Zhang, Z., Yan, X., Cheng, X., Wang, Y., Genghua, L., 2015. A kind of tungten-tin vein deposit between magmatic rock type and shear zone type. J. Guilin Univ. Technol. 35 (1), 8–14 (In Chinese with English Abstract).

Wei, W.F., Hu, R.Z., Bi, X.W., Peng, J.T., Su, W.C., Song, S.Q., Shi, S.H., 2012. Infrared microthermometric and stable isotopic study of fluid inclusions in wolframite at the Xihuashan tungsten deposit, Jiangxi province, China. Mineral. Deposita 47 (6), 589–605.

Weis, P., Driesner, T., Heinrich, C.A., 2012. Porphyry-copper ore shells form at stable pressure-temperature fronts within dynamic fluid plumes. Science 338 (6114), 1613–1616.

Williams-Jones, A.E., Migdisov, A.A., 2013. Experimental constraints on the transport and deposition of metals in ore-forming hydrothermal systems. Rev. Econ. Geol. 18, 77–95.

Wood, S.A., Spera, F.J., 1984. Adiabatic decompression of aqueous solutions: applications to hydrothermal fluid migration in the crust. Geology 12 (12), 707–710.

Wood, S.A., Samson, I.M., 2000. The hydrothermal geochemistry of Tungsten in Granitoid environments: I. Relative solubilities of ferberite and scheelite as a function of T, P, pH, and Mnacl. Econ. Geol. 95, 143–182.

Wu, M., Samson, I.M., Zhang, D., 2017. Textural and chemical constraints on the formation of disseminated granite-hosted W-Ta-Nb mineralization at the Dajishan Deposit, Nanling Range, Southeastern China. Econ. Geol. 112 (4), 855–887.

Xi, B.B., Zhang, D.H., Zhou, L.M., Zhang, W.H., Wang, C., 2008. Characteristics of ore-forming fluid evolution in Dajishan tungsten deposit, Quannan County, Jiangxi. Acta Geol. Sin. 82 (7), 956–966 (in Chinese with English abstract).

Xie, X., Liang, Ting, Lu, Lin, Zheng, Z., Zhenghui, C., Wei, C., Ming, D., 2017. Chemical composition and crystal texture of the Pangushan and Taoxikeng wolframite in southern Jiangxi and its indication significance. Acta Geol. Sin. 91 (4), 876–895 (In Chinese With English Abstract).

Xing, H.L., Makinouchi, A., 2002. Finite element modeling of thermo-elasto-plastic finite deformation and its application in sheet warm forming. Eng. Comput. 19 (4), 392–410.

Xiong, Y.Q., Shao, Y.J., Zhou, H.D., Wu, Q.H., Liu, J.P., Wei, H.T., Zhao, R.C., Cao, J.Y., 2017. Ore-forming mechanism of quartz-vein-type W-Sn deposits of the Xitian district in SE China: implications from the trace element analysis of wolframite and investigation of fluid inclusions. Ore Geol. Rev. 83, 152–173.

Yardley, B.W.D., 2005. 100th Anniversary Special Paper: metal concentrations in crustal fluids and their relationship to ore formation. Econ. Geol. 100 (4), 613–632.

Yu, C., 2004. Fractal dilation of multiple hydraulic fracturing. Earth Sci. Front. 11 (3), 11–44.

Zhang, C., 1981. The temporal and spatial characteristics of wolframite composition in the tungsten deposits in Jiangxi. Geol. Expl. 1 (2), 3–14 (In Chinese with English abstract).

Zhang, Q., Zhang, R.-Q., Gao, J.-F., Lu, J.-J., Wu, J.-W., 2018. In-situ LA-ICP-MS trace element analyses of scheelite and wolframite: constraints on the genesis of veinlet-disseminated and vein-type tungsten deposits, South China. Ore Geol. Rev. 99, 166–179.

Zhang, R.Q., Lu, J.J., Lehmann, B., Li, C.Y., Li, G.L., Zhang, L.P., Guo, J., Sun, W.D., 2017. Combined zircon and cassiterite U-Pb dating of the Piaotang granite-related tungsten–tin deposit, southern Jiangxi tungsten district, China. Ore Geol. Rev. 82, 268–284.

Zhao, B., Han, L., Pilz, J., Wu, J., Khan, F., Zhang, D., 2017a. Metallogenic efficiency from deposit to region–A case study in western Zhejiang Province, southeastern China. Ore Geol. Rev. 86, 957–970.

Zhao, C.B., Reid, L.B., Regenauer-Lieb, K., 2012. Some fundamental issues in computational hydrodynamics of mineralization: a review. J. Geochem. Explor. 112, 21–34.

Zhao, W.W., Zhou, M.-F., Li, Y.H.M., Zhao, Z., Gao, J.-F., 2017b. Genetic types, mineralization styles, and geodynamic settings of Mesozoic tungsten deposits in South China. J. Asian Earth Sci. 137, 109–140.

Zhou, L., Li, G., Wang, X., Tang, A., Wei, X., Chen, G., Liu, Z., 2017. A preliminary study of fluid inclusions of topaz crystal from Mapping tungsten deposit, southern Jiangxi Province. Mineral Deposits 36 (4), 921–934 (In Chinese with English Abstract).

Zhou, X., Burbey, T.J., 2014. Fluid effect on hydraulic fracture propagation behavior: a comparison between water and supercritical CO2-like fluid. Geofluids 14 (2),

174–188.

Zhou, X.M., Sun, T., Shen, W.Z., Shu, L.S., Niu, Y.L., 2006. Petrogenesis of Mesozoic granitoids and volcanic rocks in south China: a response to tectonic evolution. Episodes 29 (1), 26–33.

Zhu, C., Anderson, G.M., Lv, P., 2017. Theories and Applications of Geochemical Modelling. Science Press, Beijing, pp. 351.

Zhu, X., Wang, J., Wang, Y., Chen, X., Fu, Q., 2014. Relatively closed ore-forming systems in the tungsten-bearing vein: a case study of the Yaogangxian deposit, Hunan Province. Acta Geol. Sin.-Chin. Ed. 88 (5), 825–835.

Zhu, X.Y., Wang, J.B., Wang, Y.L., Chen, X.Y., Qibin, F.U., Tian, Y., 2015. The differences of the ore-forming fluid between the vein-type and skarn type tungsten deposits. Acta Petrol. Sin. 31 (4), 941–953 (in Chinese with English abstract).

Zhu, Y.L., Li, C.Y., Lin, Y.H., 1981. Tungsten Deposit Geology in South Jiangxi Province. Jiangxi People's Publishing House, Nanchang.

Zhuang, L., Kim, K.Y., Jung, S.G., Diaz, M., Min, K.-B., 2018. Effect of water infiltration, injection rate and anisotropy on hydraulic fracturing behavior of granite. Rock Mech. Rock Eng.

Zoback, M.D., Rummel, F., Jung, R., Raleigh, C.B., 1977. Laboratory hydraulic fracturing experiments in intact and pre-fractured rock. Int. J. Rock Mech. Min. Sci. Geomech. Abstracts 14 (2), 49–58.